Journal of Structural Geology 176 (2023) 104963

Contents lists available at ScienceDirect

Journal of Structural Geology

journal homepage: www.elsevier.com/locate/jsg

The kinematics of a salt sheet recorded in an array of distorted intrasalt stringers (Les Avellanes Diapir – South-Central Pyrenees)

Gabriel Cofrade [a,b,*], Prokop Závada [c], Ondřej Krýza [c], Irene Cantarero [a,b], Òscar Gratacós [a,d], Oriol Ferrer [a,d], Sadegh Adineh [c,e], Pedro Ramirez-Perez [a,b], Eduard Roca [a,d], Anna Travé [a,b]

[a] Institut de Recerca Geomodels, Universitat de Barcelona (UB), c/Martí i Franquès s/n, 08028 Barcelona, Spain
[b] Departament de Mineralogia, Petrologia i Geología Aplicada, Facultat de Ciències de la Terra, Universitat de Barcelona (UB), c/Martí i Franquès s/n, 08028 Barcelona, Spain
[c] Institute of Geophysics, Czech Academy of Sciences, Boční II 1a/1401, Prague, Czech Republic
[d] Departament de Dinàmica de la Terra i de l'Oceà, Facultat de Ciències de la Terra, Universitat de Barcelona (UB), c/Martí i Franquès s/n. 08028 Barcelona, Spain
[e] Institute of Petrology and Structural Geology, Charles University, Prague, Czech Republic

ARTICLE INFO

Keywords:
Diapirism
Diapir structure
Salt sequence
Pyrenees
Stringer

ABSTRACT

Stringers represent fragments of competent, brittle layers, formerly interstratified within a layered evaporite sequence (LES) that are entrained and deformed by viscous flow. To resolve the impact of the stringers on the deformation style of an extrusive salt sheet, an array of decameter-thick, carbonate stringers, preserved in the caprock matrix of the *Les Avellanes* Diapir (South-Central Pyrenees) was analysed. The diapir exposure was mapped in detail to produce a cross-section that shows the stringer assemblage. To understand the dynamic behaviour of stringers, this natural prototype has been reproduced using scaled analogue models. In the model, stringers were carried into the salt sheet, rotating and deforming while migrating toward the sheet front. The array of stringers can be divided into the following three structural domains: 1) a feeder domain mainly hosting vertical stringers parallel to the stem wall that rotate to a subhorizontal orientation as they approach the allochthonous sheet, 2) a sheet domain containing stack-like sets of subvertical and overturned, to subhorizontal stringers, as well as isoclinally and recumbently folded stringers, and 3) a sheet front domain characterised by stringers dipping toward the salt sheet front. Compartmentalization of the horizontal flow by the transported stringers controlled the deformation in the caprock matrix above. Finally, the similarity between the field observations and the model is evaluated and discussed to shed light on the *Les Avellanes* Diapir kinematic evolution.

1. Introduction

Salt diapirs are formed by the migration and accumulation of halite (hereafter referred to as salt) and other evaporites within different geological settings and conditions (Hudec and Jackson, 2007; Jackson and Hudec, 2017a). Many studies have been centered on a detailed characterization of the diapir adjacent stratigraphy and structure, focusing on the interplay between sedimentation and diapirism in order to unravel diapir evolution. In these studies, the internal diapir structure is often simplified and portrayed as a homogeneous body (e.g. Saura et al., 2016). This simplification is useful to highlight salt-sediment interactions as an approach to interpret the diapir structure. However, the ductile mobilization of salt disturbs the initial depositional sequence, resulting in a complex internal diapir architecture (e.g. Talbot and Jackson, 1987; Jackson and Hudec, 2017b; Hudson et al., 2017; Rowan et al., 2020; Evans and Jackson, 2021). Additionally, as salt beds within diapirs are often not well-imaged on seismic sections and surface outcrops and mine excavations present limited exposures, the internal diapir structure is usually poorly understood.

Evaporitic sequences contain intervals of halite with other interbedded evaporites and non-evaporite rocks that altogether form layered evaporite sequences (LES) (Fiduk and Rowan, 2012; Jackson and Stewart, 2017; Rowan et al., 2019). The most reported intrasalt layers are sulphates (gypsum or anhydrite), carbonates, and fine-grained siliciclastics, deposited as alternating layers with the salt in the evaporitic basin (Warren, 2010, 2016). In addition to these sedimentary layers, igneous intrusions are also common (e.g. Faramarzi et al., 2015; Martín-Martín et al., 2017; Roca et al., 2021).

* Corresponding author. Institut de Recerca Geomodels, Universitat de Barcelona (UB), c/Martí i Franquès s/n, 08028 Barcelona, Spain.
E-mail address: gcofrade@ub.edu (G. Cofrade).

https://doi.org/10.1016/j.jsg.2023.104963
Received 21 July 2023; Received in revised form 21 September 2023; Accepted 25 September 2023
Available online 4 October 2023

The interbedding of competent, non-saline layers in LES results in a stratified rheology that deforms with the salt flow (Rowan et al., 2019; Evans and Jackson, 2021) usually disrupting these layers into fragments, named stringers (Strozyk, 2017). Stringers display many different patterns of deformation acquired during the complex flow that spans from the in situ LES to the diapir. The regional stress regime, the competence contrast between strong and weak layers, the deformation rate, and the relative thickness of these competent layers control the deformation style of the stringers and affect the salt flow (Jackson and Hudec, 2017b). Therefore, studying the array of stringers is a direct method to explore the internal deformation of diapirs as a consequence of salt flow dynamics. In this regard, the stringers: 1) produce acoustic horizons that can be seismically traced along the interior of salt structures (except where they are vertically oriented) (Van Gent et al., 2011; Cartwright et al., 2012; Strozyk et al., 2012; Strozyk, 2017; Fiduk and Rowan, 2012; Jackson et al., 2014), 2) are usually exposed in mine excavations (Burliga, 1996; Burliga et al., 2005; Schléder et al., 2008; Jackson et al., 2015; Rowan et al., 2020), 3) can be mapped on exposed salt structures (Talbot and Aftabi, 2004; Al-Siyabi, 2005; Reuning et al., 2009; Schoenherr et al., 2010; Rowan and Fiduk, 2015; Hudson et al., 2017; Kernen et al., 2019; Závada et al., 2021; Cofrade et al., 2023a,b), and 4) their polarity with respect to the original orientation of the sedimentary bedding can be sometimes identified (Burliga, 1996).

Furthermore, as the mobilized LES approaches the surface, halite and other highly soluble evaporites are dissolved by undersaturated fluids. The residue formed after their dissolution and the subsequent accumulation of non-dissolved materials is usually named salt caprock (Posey and Kyle, 1988; Jackson and Lewis, 2012; Kernen et al., 2019). This caprock grows thicker by integrating these non-dissolved impurities, forming a soft, mainly sulphate residue, termed caprock matrix (Hudson et al., 2017; Závada et al., 2021). If present, decameter-thick, laterally extensive and significantly more resistant stringers (i.e., anhydrite, carbonate, and/or sandstone stringers) can be incorporated within the caprock matrix as it grows over time.

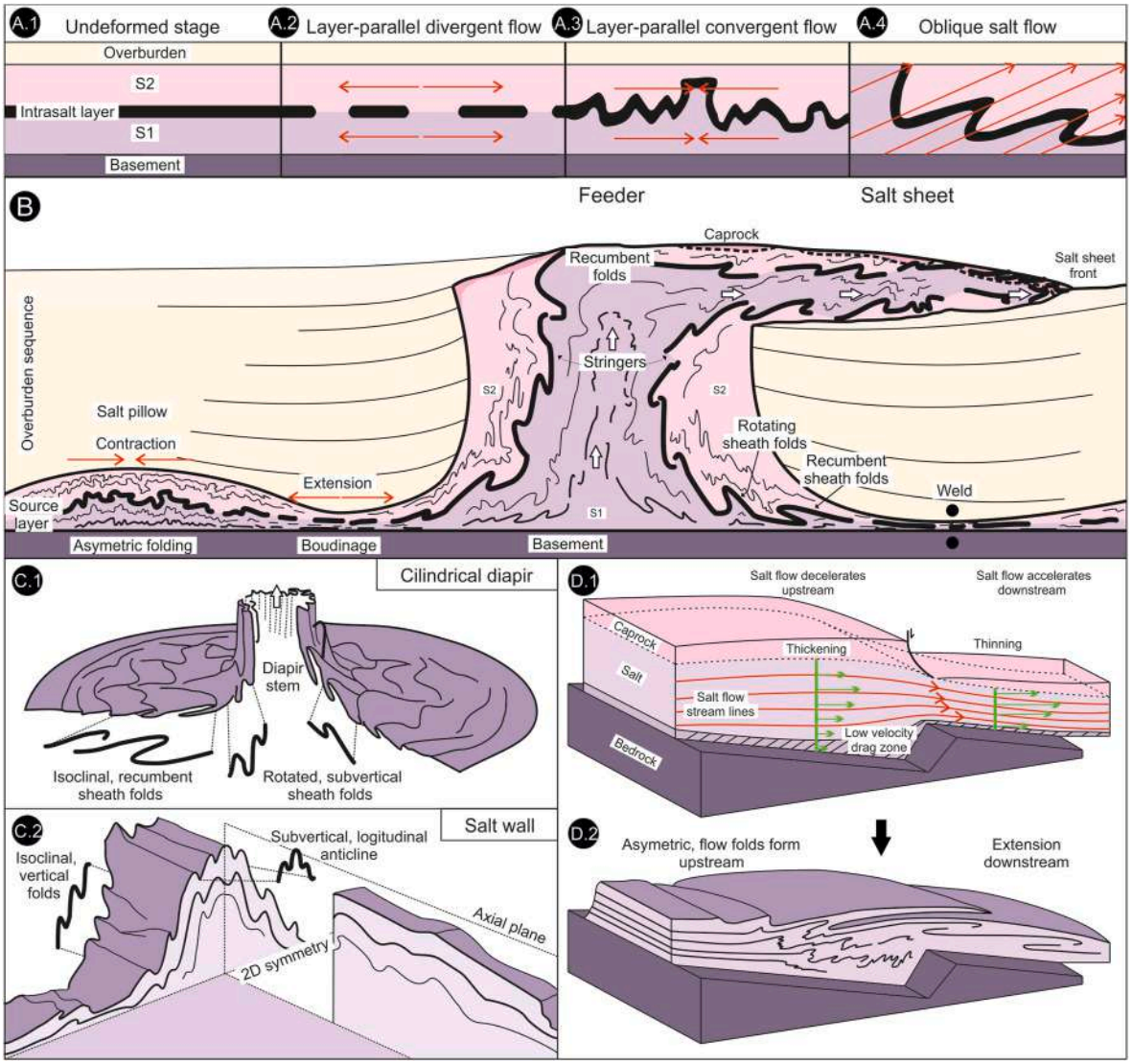

Fig. 1. (A) Sketches representing a layered salt sequence with two salt intervals separated by a competent layer (modified from Jackson and Hudec, 2017b). (A.1) Undeformed stage. (A.2) Layer-parallel, divergent salt flow causes the stretching and rupture of the intrasalt layer. (A.3) Layer parallel, convergent salt flow causes compression and the formation of asymmetrical folds. (A.4) Oblique salt flow relative to the intrasalt layer. (B) Sketch representing a 2D section of a typical salt structure focused on the deformation style of the intrasalt layers. (C.1) Internal deformation within a 3D cylindrical diapir or salt stock (after Talbot and Jackson, 1987). (C.2) Internal deformation along a salt wall. (D.1) Section of the salt flow in an extrusive salt sheet/salt glacier representing an irregular bedrock. Green arrows represent flow velocity (after Talbot and Pohjola, 2009). (D.2) Same section as in D.1 representing the deformation of salt layers compared with the salt flow. (For interpretation of the references to colour in this figure legend, the reader is referred to the Web version of this article.)

If the caprock is not affected by intense and pervasive deformation (as in diapiric breccias, e.g. Leach et al., 2016) and/or diagenetic transformations that mask the diapir internal structure, the array of more competent stringers potentially retain the structural configuration given by the salt flow (Talbot and Jackson, 1987; Jackson et al., 2015). Therefore, these stringers preserved within the caprock matrix may function as strain markers, and thus, serve as a proxy to constrain the diapir evolution.

The deformation attributed to a flowing LES has classically been explored using numerical (Koyi, 2001; Chemia et al., 2008; Chemia and Koyi, 2008; Li, 2012; Li et al., 2012; Fuchs et al., 2015), conceptual (e.g. Rowan et al., 2019), and analogue models, owing to the scarcity and limitations of seismic images and outcrops. Between them, analogue models represent an empirical approach to reproduce a wide range of salt architectures and can provide guidelines for a better understanding of major field observations (e.g. Escher and Kuenen, 1929; Cartwright et al., 2012; Warsitzka et al., 2015; Pichel et al., 2019).

The deformation of LES (Fig. 1A.1) starts from a pre-diapiric stage as salt is perturbed by differential loading or tectonics strains (Hudec and Jackson, 2007; Rowan et al., 2019). In a generalized scheme, below sinking depocenters, salt deflation causes layer-parallel stretching, resulting in the fragmentation of the more competent intrasalt layers, which form the stringers (Fig. 1A.2) (Van Gent et al., 2011; Rowan and Fiduk, 2015; Strozyk, 2017). Alternatively, within the core of salt-detached anticlines/salt pillows, convergent salt flow results in buckle folding and thrusting of the LES (Fig. 1A.3) (Van Gent et al., 2011; Jackson et al., 2014, 2015; Pla et al., 2019; Rowan et al., 2019). When salt flow is oblique to the layering, a superimposed, asymmetric folding is generated (Fig. 1A.4).

During and following diapir initiation, stringers can be transported by the salt flow into the diapir (Fig. 1B) (Jackson and Hudec, 2017b). The entrainment potential for the stringers within a diapir reflects the balance between the flow velocity of the host salt in the diapir, and the size and density of the stringers (Li et al., 2012; Fuchs et al., 2015). In turn, primary parameters asserting control on the flow of salt are: 1) differential loading, and 2) external tectonic forces. Additionally, the bulk properties of the LES are affected by its stratigraphical architecture (Chemia and Koyi, 2008; Li, 2012; Peel et al., 2020).

In the diapiric stage, flow dynamics, and therefore, the deformation style of the stringers, is strongly impacted by the geometry of the structure (axial symmetric vs. wall-shaped diapirs) (Fig. 1C.1-C.2) (Talbot and Jackson, 1987; Chemia et al., 2008; Sarkarinejad et al., 2018). When diapirs take on a cylindrical shape they induce a flow that converges radially at the base producing constriction associated with curtain-style folding of the embedded stringers (Fig. 1C.1) (Sarkarinejad et al., 2018). However, the general pattern observed in salt walls is simpler than in the cylindrical diapirs, therefore, the internal strain and distortion of the stringers can be described in 2D symmetry (Jackson et al., 2014, 2015) (Fig. 1C.2). At the vent of the diapir, horizontally spreading flow over the surface induce the refolding of the stringers from near-vertically oriented stringers into recumbent folds with near-horizontal axial planes (Fig. 1B) (Jackson and Hudec, 2017b).

If the salt supply rate in a surfacing diapir surpasses the sedimentation rate, salt emanates from a feeder diapir, creating an extrusive allochthonous structure named salt sheet or salt glacier (Fig. 1B) (Talbot and Pohjola, 2009; Jackson and Hudec, 2017b). The pressure caused by the rising salt sustains a dynamical bulge over the diapir vent that collapses toward adjacent low areas (Dooley et al., 2015). The rate of advance and the area covered by the allochthonous sheet depend on the local sedimentation rate, the dissolution rate of the salt, and the topography of the adjacent area (McGuiness et al., 1993; Hudec and Jackson, 2006; Peel et al., 2020). Within the spreading of an extrusive salt sheet, the frictional drag along the salt-bedrock interface creates the classical Couette flow profile with faster displacement velocities at the top surface of the extrusion (Talbot and Pohjola, 2009; Pichel et al., 2019). In addition, irregularities of the salt-bedrock interface locally affect the velocity profile across the extruding salt sheet and thus, create oscillations in the flow velocity (Talbot, 1979; Talbot and Jackson, 1987). Upstream from a bedrock ridge, the streamlines diverge, so salt decelerates and thickens (Fig. 1D.1), inducing the horizontal shortening of the cover (Fig. 1D.2). Contrary, downstream the streamlines converge (Fig. 1D.1) and salt accelerates inducing downslope oriented stretching (Fig. 1D.2) (Dooley et al., 2017).

Stringers can also be extruded from a feeder and carried with an advancing allochthonous sheet. Moreover, a caprock may form during the advance of subaerial extrusions as halite and highly soluble evaporites are progressively dissolved. The effect of the stringers on the flow kinematics, the deformation style, and the strain distribution within an advancing salt sheet are not understood and have not been reliably addressed yet in any modelling or field study. Similarly, neither the entrainment potential and transport of stringers in extrusive salt sheets nor the deformation of the caprock associated with these salt structures during the allochthonous advance are well understood.

In this framework, we aim to focus on the style of stringer deformation in a viscous salt sheet through field-based-structural mapping of a uniquely exposed stringer array in the *Les Avellanes* Diapir (South-Central Pyrenees) together with a complementary scaled analogue modelling study. In this diapir, the lack of localised deformation inside the carbonate stringers and the surrounding caprock matrix suggests that the arrangement of these stringers was produced by salt flow during the salt sheet emplacement and then was preserved within the caprock. Moreover, the characterization of these stringers allows us to build a careful reconstruction of the stringer's polarity from original sedimentary bedding markers or from the superposed stratigraphical subunits that form these stringers. In this sense, to decipher the structural configuration of the stringers during the salt sheet advance relative to the dynamic characteristics of the viscous flow as well as the associated deformation in the caprock, an analogue modelling was performed. Accordingly, the comparison between the *Les Avellanes* Diapir natural prototype and the experimental setup allows for a better interpretation of the internal structure and kinematics of, not only the allochthonous salt body of this specific diapir, but for the stringer-bearing viscous salt sheets in general.

2. Geological setting

The *Les Avellanes* Diapir outcrops in the frontal part of the South-Central Pyrenean Fold-and-Thrust Belt (SCPB). The Pyrenees is an Alpine orogen created by the subduction and subsequent collision of the Iberian plate with the European plate, from Late Cretaceous to Miocene times (Muñoz, 1992; and 2002; Vergés et al., 2002; Pedreira et al., 2003; Chevrot et al., 2015). The Pyrenean orogen consists of a hinterland backbone, called the Axial Zone, flanked by two opposite-verging fold-and-thrust belts (Fig. 2A) (Muñoz, 1992; Vergés et al., 2002). The SCPB is an orogenic wedge decoupled over the Middle to Upper Triassic LES and emplaced over the autochthonous sedimentary sequence of the Ebro Foreland Basin (Fig. 2B) (Séguret, 1972; Vergés and Muñoz, 1990; Beaumont et al., 2000). The SCPB is formed by three main thrust sheets developing in sequence as the orogenic contraction propagated southwards from the Axial Zone (Muñoz, 1992, 2002). These are, in order of emplacement, the Bóixols/Cotiella Thrust Sheet (Late Cretaceous), the Montsec/Peña Montañesa Thrust Sheet (Paleocene-early Eocene), and the Serres Marginals Thrust Sheet (Eocene-Oligocene) (Fig. 2C) (Beaumont et al., 2000; Garcés et al., 2020; Cruset et al., 2020; Muñoz-López et al., 2022).

The distribution and mobilization of the Triassic salt play a core role in the mountain-building processes along the South-Central Pyrenean belt (Beaumont et al., 2000; Camara and Flinch, 2017; Muñoz et al., 2018). The Middle to Upper Triassic salt acts as a major décollement and controls the thin-skinned deformation style of the overlying cover. The Triassic crops out in the core of the anticlines and the base of exposed thrusts, and forms diapirs mainly located at the edges of the major thrust

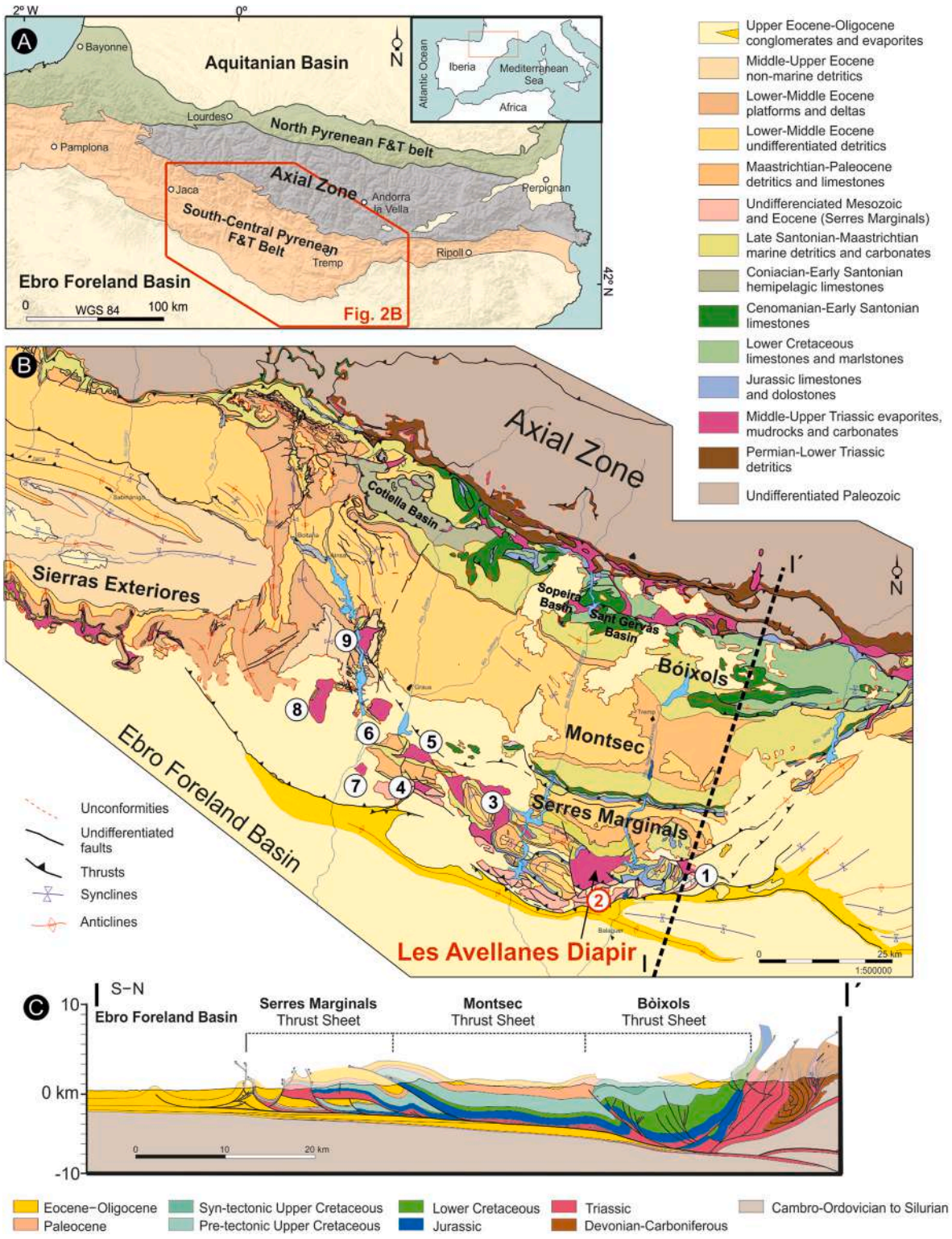

Fig. 2. (A) Simplified map of the Pyrenees and geographic landmarks (Modified from González-Esvertit et al., 2022, 2023). (B) Geological map of the South-Central Pyrenean Fold-and-Thrust Belt (after Cofrade et al., 2023a, modified from Muñoz et al., 2018) highlighting the location of the main diapirs of the Serres Marginals Thrust Sheet. 1) Alòs de Balaguer, 2) Les Avellanes Diapir, 3) Estopinyà, 4) Calasanz, 5) Justeu, 6) La Puebla de Castro, 7) Estada, 8) Naval diapir, and 9) Clamosa. (C) Cross-section of the South-Central Pyrenean Fold-and-Thrust Belt (after Muñoz et al., 2018). See location in (B).

sheets (García-Senz, 2002; Muñoz et al., 2018; Casini et al., 2023) (Fig. 2B–C). Diapirism has been previously studied in the northern areas of the SCPB, (e.g. Cotiella basin, Lopez-Mir et al., 2015, 2016; Sopeira-Sant Gervàs basins, Saura et al., 2016; Organyà basin, García--Senz, 2002; Casini et al., 2023) where diapirism started during the Early Cretaceous rifting stage with later growth during the middle to Late Cretaceous post-rift phase. However, it has been proposed that this diapirism could have started earlier in pre-orogenic times during a Jurassic rifting phase (Burrel and Teixell, 2021; Hudec et al., 2021).

Along the southern Serres Marginals Thrust Sheet, where the *Les*

Avellanes Diapir is located, there are several other diapirs mostly associated with syn-orogenic deformation (Fig. 2) (e.g. Naval diapir, Santolaria et al., 2014). The evacuation of salt parallel to the shortening direction probably favoured the formation of diapirs and salt extrusions in the external part of the SCPB as syn-orogenic deformation and sedimentary loading expulsed the salt forelandward (Cofrade et al., 2022). Diapirism along these external areas of the SCPB was probably triggered by radial extension along the curved thrusts (Muñoz et al., 2013), and the erosion and/or crestal stretching of contractional anticlines (Teixell and Barnolas, 1995; Muñoz et al., 2013; Santolaria et al., 2014).

The *Les Avellanes* Diapir comprises at the surface a mixture of gypsum and mudrocks that enclose decameter to kilometer-sized fragments of tabular upper Muschelkalk carbonates (M3), dolerites, and more locally, red mudrocks with gypsum interbeds (Salvany and Bastida, 2004; Calvet et al., 2004; Cofrade et al., 2023a,b). Dolerite intrusions in the form of dykes and sills were emplaced after LES deposition during the Middle to Late Triassic (Fig. 3) (Calvet et al., 2004; López-Gómez et al., 2019; Ayala et al., 2021). Although salt (halite) is not found at the surface, gravimetric studies (Santolaria et al., 2016, 2021) and salty springs (Vilanova de la Sal springs, at the *Les Avellanes* Diapir) reveal the existence of subsurface accumulations of salt beneath the diapir exposure. In addition, wells penetrating the Triassic sequence in the Ebro Foreland Basin encountered two main salt successions located in the Middle Triassic (middle Muschelkalk facies, M2) and in the Upper Triassic (middle Keuper facies, K1–K2) respectively. Both successions also include intervals of mudrocks and interbeds of anhydrite. The two main salt successions are separated by a decameter-thick carbonate interval from the upper Muschelkalk facies (M3, Middle-Upper Triassic) (Fig. 3) (Lanaja, 1987; Klimowitz and Torrescusa, 1990; Ortí et al., 1996; Camara and Flinch, 2017). Accordingly, the surface exposure of the *Les Avellanes* Diapir is interpreted as a caprock residue accumulated by the dissolution of both, the middle Muschelkalk and the lower Keuper salt. This caprock contains a matrix formed of strongly dismembered beds of mudrocks and former anhydrite (transformed into gypsum at the surface) that encloses the decameter-thick and laterally extensive stringers from the M3 interval, as well as bodies of dolerites and stratified mudrocks (Cofrade et al., 2023a). The M3 carbonate stringers are the main focus of this work.

Flanking the *Les Avellanes* Diapir, the overburden stratigraphy is divided between the pre-orogenic, and the syn-orogenic sequences (Fig. 3). The pre-orogenic sequence spans from the uppermost Triassic to the Jurassic. The Upper Triassic strata, forming the roof of the salt, comprise marlstones and dolostones overlain by limestones. Overlaying the Upper Triassic, the Jurassic succession evolves vertically from breccias and evaporites to marine limestones and marlstones (Fig. 3) (Pocoví, 1978; Ullastre and Masriera, 2004). The syn-orogenic sequence ranges from the Upper Cretaceous to the Oligocene. The Upper Cretaceous is mainly formed of calcareous sandstones (Calcària de les Serres

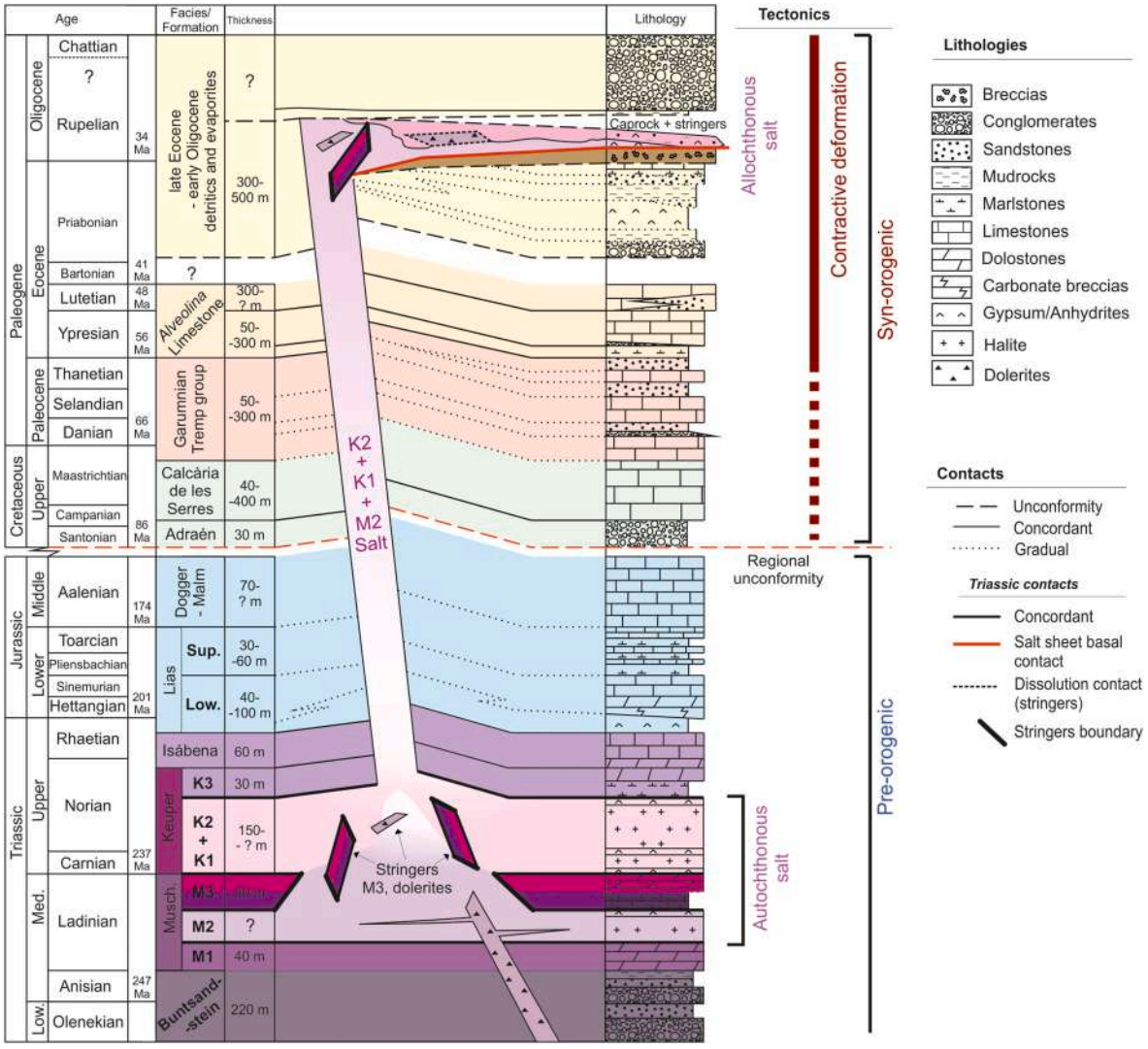

Fig. 3. Simplified stratigraphical sketch of the *Les Avellanes* Diapir and adjacent areas (modified from Cofrade et al., 2023b).

Fm.) with basal quartz-rich conglomerates, named the Adraén Fm. Above, the uppermost Cretaceous gradually passes into a Paleocene alternation of lacustrine limestones and sandstones (Tremp Group). The overlying lower Eocene is again marine (*Alveolina* Limestone facies) and consists of limestones displaying syn-orogenic growth-strata geometries. Its top is an unconformity covered by upper Eocene-Oligocene continental deposits that are also discordant over older units. The base of the upper Eocene-Oligocene is mainly formed by evaporites and conglomerates deposited in partially isolated orogenic sub-basins (Teixell and Muñoz, 2000). The top of the Oligocene is represented by an alluvial conglomeratic succession (reaching a minimum thickness of 700 m in the study area), which recorded the uplift and erosion of the Axial Zone. These Oligocene conglomerates postdate the tectonic structures in the study area (Fillon et al., 2013) as well as the *Les Avellanes* Diapir (Fig. 3). Separating the pre-orogenic and the syn-orogenic sequences, there is a regional unconformity whose stratigraphical gap decreases northward where the overburden units become thicker and more complete (Fig. 3). This unconformity formed at the onset of contractional deformation (Santonian-Late Cretaceous) and was associated to the lithospheric flexure of the Iberian plate beneath the growing Pyrenean orogen. This flexure resulted in the uplift of the pre-orogenic rocks at the forebulge areas (present position of the Serres Marginals) and the subsequent incision of the syn-orogenic units on the external tip of the former South Pyrenean Foreland Basin (Muñoz et al., 2018).

The interpretation of the overburden stratigraphy, as well as the adjacent tectonic structures and tectonosedimentary relationships, shed light on the *Les Avellanes* Diapir geometry and evolution. The *Les Avellanes* Diapir is located in the intersection of two structural domains in which the tectonic structures affecting the meso-Cenozoic salt-detached cover have different trends: 1) an eastern domain where ENE folds and thrusts prevail and 2) a western domain where folds and thrusts have a main NW trend (Fig. 4A). The outcropping body of the *Les Avellanes* Diapir fossilizes both different trending structures except at its northern edge, where two sets of south-dipping extensional faults (ENE-WSW and NW-SE) constitute the northern diapir contact and extend outward from the diapir exposure (Cofrade et al., 2023b). The hangingwalls associated with both sets of extensional faults are filled by upper Eocene-Oligocene conglomerates, which also postdate these faults at the NE area. Accordingly, they are interpreted as syn-orogenic faults. Additionally, the uppermost part of the conglomerate succession onlaps the diapir body in the NE and NW boundaries.

In the southern boundary, the diapir body covers an upper Eocene-Oligocene succession that comprises evaporites and conglomerates. At the SW boundary, these successions were interpreted as a record of the advance of an extrusive salt sheet/salt glacier (Cofrade et al., 2023a). As the diapir body covers similar facies along the southern diapir boundary, this contact was interpreted and mapped as the base of this salt sheet. Therefore, a feeder diapir was probably located along the northern area (Cofrade et al., 2023b).

Taking into account these observations, the diapir evolution is interpreted as follows. The mobilization of the Triassic LES in the study area was probably associated with the onset of syn-orogenic deformation in the Serres Marginals, which occurred during the lower Eocene (Muñoz, 2017). During the middle to late Eocene forelandward migrating salt was accumulated in the anticline cores, expulsed from the tectonic development of SCPB. During the late Eocene, the erosion of a salt-cored anticline crest located along the northern diapir boundary triggered diapirism (Cofrade et al., 2023a). The squeezing of the diapir and the subsequent increase in the salt supply rate caused by the ongoing Pyrenean contraction provoked the allochthonous advance (Fig. 4, B.1). This increasing salt supply rate also caused the subsequent migration of the salt toward the diapir body creating the aforementioned sets of extensional faults (Cofrade et al., 2022). Therefore, the salt advanced southward in subaerial conditions as an extrusive salt sheet, covering the adjacent low areas (Fig. 4, B.2). Finally, the salt extrusion is postdated by Oligocene conglomerates that onlap the diapir along its NW and NE areas (Fig. 4, B.3), pointing toward the welding of the diapir stem during the Oligocene. Thus, the *Les Avellanes* Diapir geometry is interpreted as a diapir stem that feeds a southward advancing salt sheet or salt glacier (Cofrade et al., 2023b).

3. The *les Avellanes* diapir exposure

The *Les Avellanes* Diapir exposure includes competent bodies, such as the M3 stringers, and soft caprock matrix of two main facies.

3.1. Competent bodies

Up to 50 competent bodies are exposed along the surface of the *Les Avellanes* Diapir. These bodies include M3 stringers, stratified mudrock intervals, and dolerite intrusions.

M3 stringers are decameter to kilometer long, up to 40 m-thick, tabular bodies of limestones or dolostones embedded within the evaporitic caprock matrix (Fig. 3). Stratigraphically, they are usually formed by a lower and an upper interval. The lower interval is formed by laminated mudstones intercalated with millimeter to centimeter-thick layers of marlstones, with a characteristic slate-like fissility (Fig. 5A). Parallel lamination, bioturbated textures, and desiccation cracks are typically observed in this interval (Fig. 5B). The upper interval is formed by well-bedded mudstones and sometimes dolostones. Packstones and wackstones of peloids, arranged in 0.5–1.5 m-thick tabular packages (Fig. 5C) are also found in certain levels. Beds show mainly planar lamination, although low-scale, trough cross-bedding, is sometimes observed (Fig. 5D). Both lower and upper intervals have been interpreted as inter-to supra-tidal carbonate ramps laterally associated with evaporitic environments (Salvany and Bastida, 2004).

Mudrock intervals preserving stratified facies are also present, sometimes attached to the M3 stringer's boundaries. These mudrocks often show parallel lamination and can contain intercalated with beds of carbonates (Fig. 5E). Similar mudrock intervals are found in both the Muschelkalk and Keuper intervals, so the precise age within the Triassic LES cannot be determined with confidence.

Dolerites form massive, decameter-sized bodies with rounded morphologies (Fig. 5F) that are embedded within the evaporitic caprock matrix. Dolerites are mainly constituted by augite and plagioclase, with doleritic textures that sometimes become more ophitic towards their boundaries. Dolerite bodies are commonly found within most of the Pyrenean Triassic diapirs, where they sometimes preserve a contact aureole surrounding the host rock. They are interpreted as a network of sills and dykes intruding early after the deposition of the LES during the Middle-Upper Triassic (Lago-San José et al., 1999).

3.2. The Les Avellanes Diapir caprock matrix

Caprock matrix forms the cohesive, generally soft material of the *Les Avellanes* Diapir in which the M3 stringers are enclosed. The caprock is mainly made of gypsum mixed with disaggregated intrasalt beds of mudrocks and carbonates, forming centimeter to milimiter-sized fragments embedded within the gypsum. The proportion of mudrocks and carbonates within the caprock matrix gradually changes from North to South. For simplicity, we define two distinct facies 1) "pure gypsum caprock" and 2) "dirty gypsum caprock".

The pure gypsum caprock has centimeter-thick, coloured bands of gypsum with elongated gypsum nodules mainly oriented according to the bands and sometimes is associated with intercalated millimeter-thick micrite layers (Fig. 6A–B). These facies are found only in the northern part of the diapir exposure. In contrast, the dirty gypsum caprock shows centimeter to meter-scale clasts of mainly mudrocks and carbonates, embedded within the gypsum. The presence of these clasts gives a characteristic reddish coloration to these facies (Fig. 6C). At the microscale, the dirty gypsum caprock is characterised by the existence of micrite replacing the gypsum crystals. This process is incomplete and

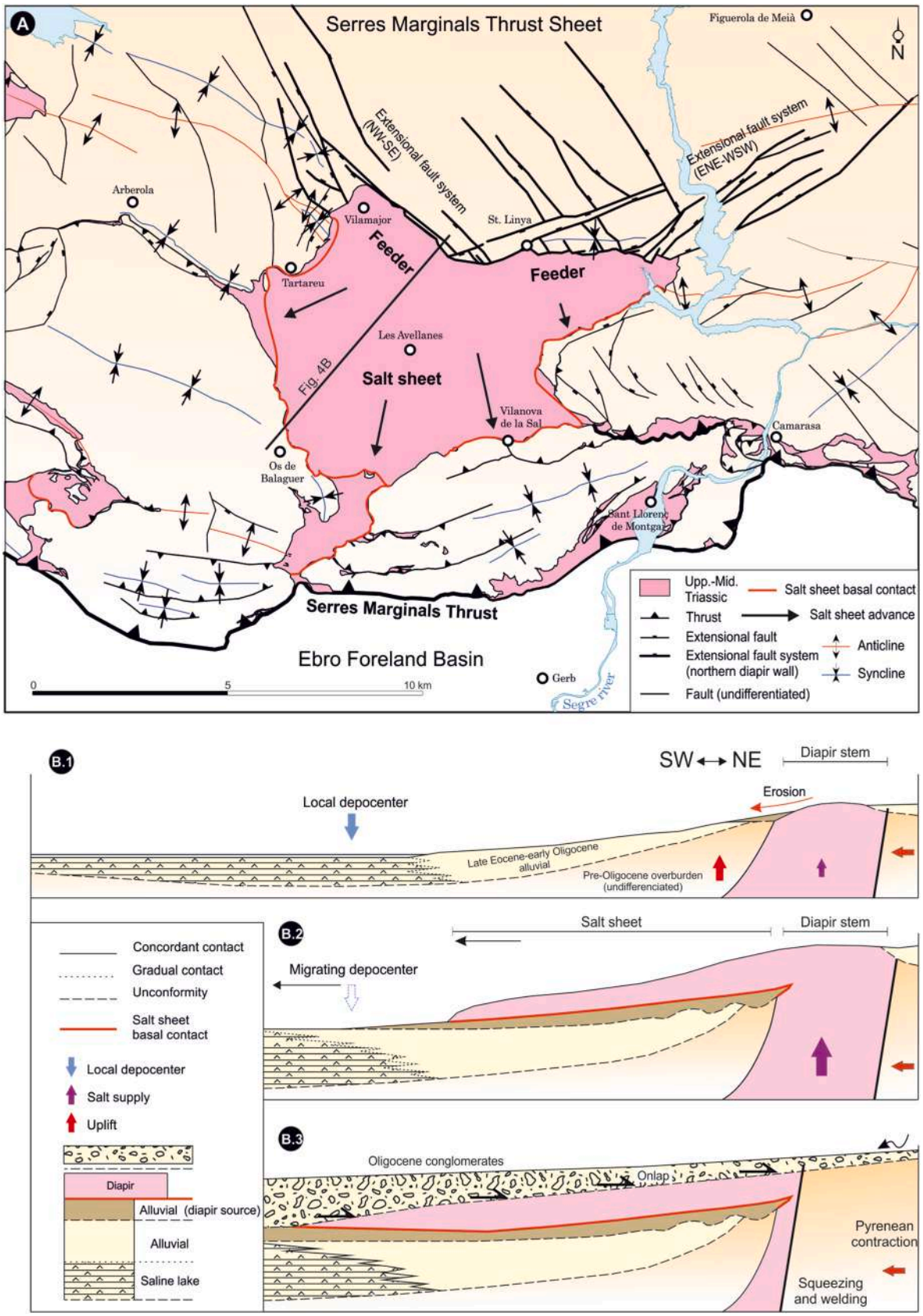

Fig. 4. (A) Structural map of the *Les Avellanes* Diapir and adjacent areas. The black line represents the approximate trace of the conceptual cross-sections represented in B. (B) Not-to-scale conceptual model showing the emplacement of the salt sheet as inferred by the sedimentological, stratigraphical and structural study of the facies along the adjacent sub-basins (Modified from Cofrade et al., 2023a). (B.1) Pre-extrusion stage. (B.2) Syn-extrusion stage. (B.3) Post-extrusion stage.

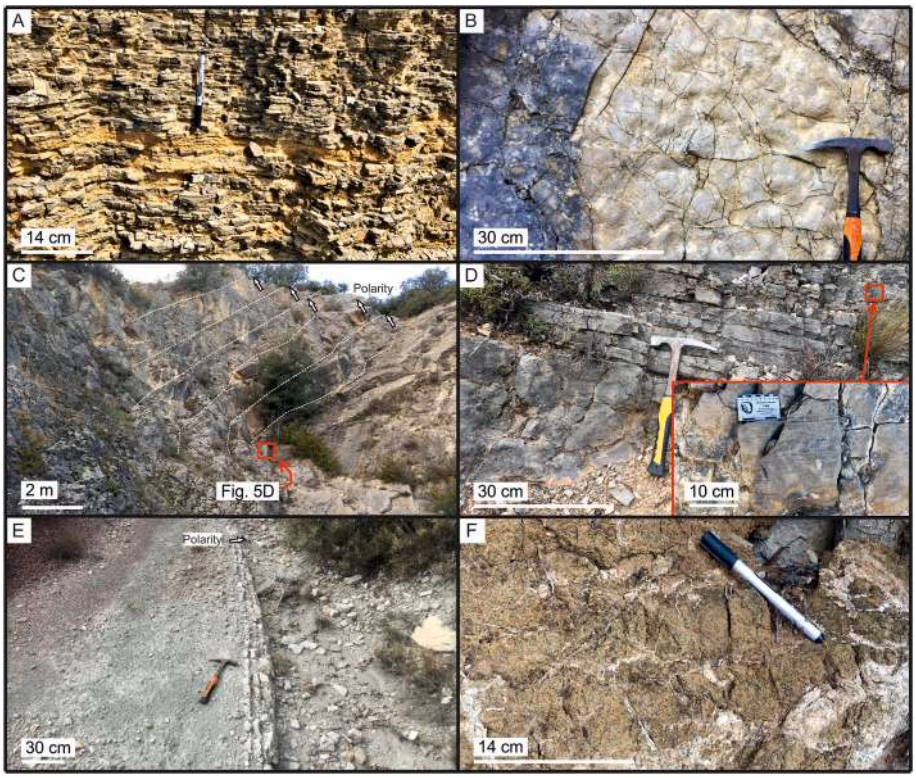

Fig. 5. (A) Muschelkalk carbonate stringers, M3, lower interval. Fine laminated rhythmic intercalation between limestones and mudrocks. (B) Muschelkalk carbonate stringers, M3, lower interval. Desiccation cracks, basal view. These sedimentological features indicate the stratigraphical polarity. (C) Muschelkalk carbonate stringers, M3, upper interval. Tabular beds of limestones. (D) Detail of the top of one of the beds shown in C with their characteristic planar lamination and small-scale cross-bedding. (E) Mudrocks with laminated carbonates intercalated. (F) Dolerites, close-up view. Chaotically oriented fractures are filled with white sulphate cement.

micrite is preferentially accumulated along the margins and exfoliation planes of the crystals (Fig. 6D). Dirty gypsum caprock crops out, in the central and southern regions of *the Les Avellanes* Diapir. In addition, in the southern boundary of the diapir and bounded to the base of the allochthonous contact, there is a megabreccia made of meter-sized, banded gypsum and M3 blocks floating in a fine-grained, sulphate-rich matrix (Fig. 6E). Moreover, also in the diapir southern boundary, the dirty gypsum caprock, frequently contains carbonate breccias, which usually appear in elongated blocks. Some of these blocks can have a tabular geometry, although such bodies have limited lateral continuity. They are characterised by moldic porosity created by the dissolution of clasts (Fig. 6F).

3.3. Les Avellanes Diapir internal structure

Deformation of the *Les Avellanes* Diapir exposure shows different styles in the caprock matrix and the more competent M3 carbonate stringers, that change along the diapir exposure. In this section, the deformation and structural configuration of M3 stringers is presented and compared with the deformation observed in the caprock matrix. However, the deformation of dolerite bodies is not analysed since these bodies do not show internal markers that can be used to decipher their internal structure.

3.3.1. M3 stringers structure and deformation

Internal deformation of the carbonate M3 stringers is controlled by the Muschelkalk stratigraphy that accommodates deformation at different scales. In the lower interval of the M3 stringers, which is formed by alternating thin-bedded laminated limestones with thinner marlstone intercalations, deformation mainly consists of pervasive centimeter-spaced joints in the limestone layers and apparently non-systematic fractures. Locally, decimeter to meter-sized, tight folds with a frequent kink geometry are present. In the upper interval, characterised by thick-bedded limestones, deformation is defined by more spaced joints and sometimes decameter-sized folds. The interlimb angle of such folds is usually larger than in the laminated limestones of the lower interval. Thrust faults with a centimetric to metric displacement are sometimes observed. These faults are usually detached at the boundary between the lower and the upper interval of the M3 succession that sometimes acts as a major décollement, dividing the M3 stringers. Usually, these individualized stringers only preserve the upper interval of the M3 carbonate succession. Additionally, M3 stringers often appear brecciated along their boundaries and the grade of deformation is gradually reduced inward. By analysing the structural configuration and the geometry of the M3 stringers, and considering both lower and upper intervals, the internal structure of the *Les Avellanes* Diapir emerges (Fig. 7).

The M3 stringers are unevenly distributed along the diapir exposure. Along the diapir northern boundary, only few stringers are exposed and they are separated by hectometer-long distances. Additionally, M3 stringers and dolerite bodies are mostly absent south of the inward-oriented promontory, where the ENE-WSW and NW-SE bounding faults join. However, in the central and southern areas, stringers are much less separated or appear in direct contact, even showing stack-like accumulations. As shown in Fig. 7, in the central areas of the diapir exposure, elongated M3 stringers show NW-SE or ENE-WSW trends, whereas the M3 stringers located in the southern part of the diapir exposure tend to be parallel to the diapir southern boundary. The M3 stringers have a planar geometry with both normal and reverse polarities, sometimes presenting fold geometries. These folds show interference folding patterns and they include upright anticlines, synclines, and anticline synforms as well as gently inclined, southward verging, tight

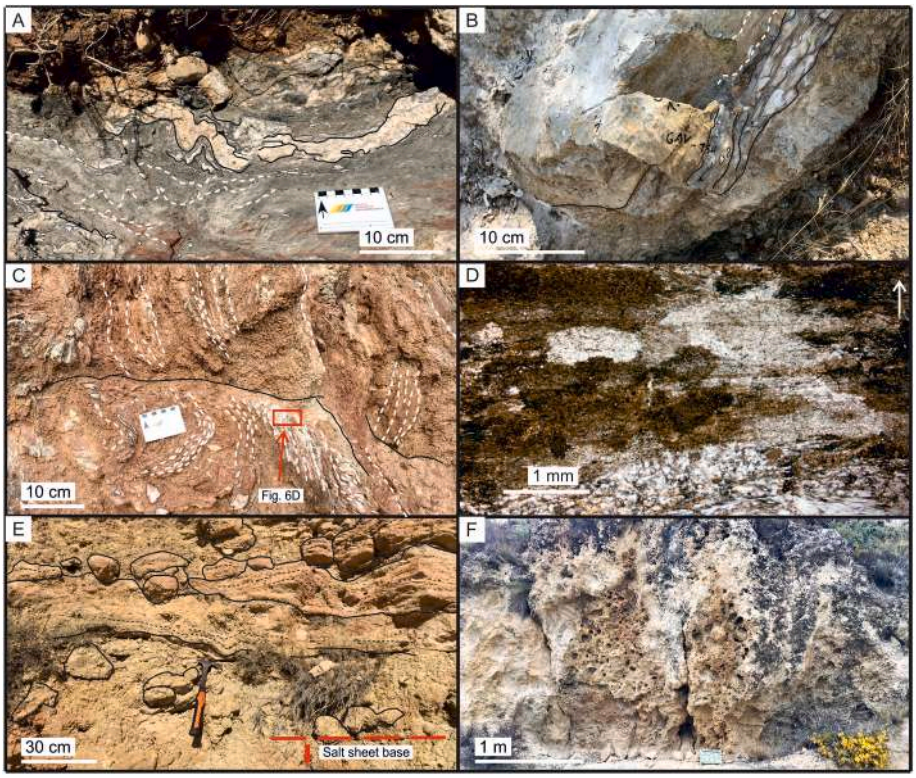

Fig. 6. (A) Pure gypsum caprock. Note the existence of folded white gypsum nodules. (B) Pure gypsum caprock. Banded facies with elongated gypsum nodules. (C) Dirty gypsum caprock. The presence of red mudrocks embedded within the gypsum coloured these facies. Folded planes (white lines) correspond to laminated gypsum and carbonates fragments. (D) Microphotograph of the laminae visible in C, crossed-polarised light. Gypsum crystals are partially replaced by micrite following the exfoliation planes of the crystals. (E) Megabreccia made of laminated gypsum blocks embedded within a fine matrix. (F) Dolostones breccias with centimeter-size moldic porosity. (For interpretation of the references to colour in this figure legend, the reader is referred to the Web version of this article.)

folds. These southward-verging folds predominate along the southern boundary of the diapir (Fig. 7).

The structural architecture of the M3 stringers has been studied in a NE-SW oriented cross-section that traverses the western part of the diapir exposure (Fig. 8). This cross-section reveals the existence of several structural domains that complement the map view and are linked to the diapir main structure. From North to South, the domains are as follows:

1) Northern domain with vertical stringers. The relatively few M3 stringers outcropping in this domain appear at the NW and NE boundaries (Fig. 7), where they form a set of near-vertical stringers oriented matching the trace of the extensional faults that form the northern diapir contact (see stereoplot 9 in Fig. 7). These stringers are separated by a pure gypsum caprock matrix.
2) Central domain with subhorizontal or subvertical sets of stacked stringers. a) The subhorizontal stacked stringers predominate near the northern domain (Fig. 7, stereoplots, 7–8). They show large plates of subhorizontal beds with a normal polarity that forms stack-like accumulations. Very locally, these stringers are affected by tight, predominantly south-verging folds (Fig. 8). b) The steeply dipping stringers are mainly present in the central and southern areas of this domain (Fig. 7, stereoplot 4). Unlike the subhorizontal ones, they show a reverse polarity and locally, these stringers are folded by tight, usually faulted steeply inclined folds (Fig. 8). The subhorizontal and the steeply dipping stringers form juxtaposed sets and are separated by the dirty gypsum caprock.
3) Southern domain with imbricated stringers. Towards the southern diapir boundary, overlapping the late Eocene-early Oligocene syn-kinematic sediments (Fig. 7), the M3 stringers are arranged in an imbricate thrust system (Fig. 9), verging toward the diapir edge (Fig. 7, stereoplots 1–3). These structures extend from the central domain to the southern boundary of the diapir (Fig. 8). The M3 stringers in this domain are again separated by the dirty gypsum caprock.

3.3.2. *Les Avellanes Diapir caprock matrix deformation*

The pure gypsum and the dirty gypsum caprocks within the *Les Avellanes* Diapir exposure contain bands (Fig. 6A), as well as elongated gypsum nodules that define planar fabrics (Fig. 6B) somewhere deformed into folds or by fractures (Fig. 6C). Folds appear in sets of asymmetric, disharmonic arrays, ranging from centimeter to meter in size (Fig. 6A), resembling flow structures. Fractures are filled with fibrous gypsum cement, either cross-cutting or parallel to the caprock fabrics, and often present apparently chaotic orientations. However, unlike the stringers, the deformation in the caprock matrix is only locally developed, and the structural orientations significantly change at the outcrop scale.

4. Analogue modelling

An experimental program was designed according to the parameters of our field prototype, the *Les Avellanes* Diapir, to simulate the transport and expulsion of stringers from a vertical diapir stem into a spreading allochthonous salt sheet. The aim is to test the configuration of stringers as being a result of dynamically evolving salt flow inside an extrusive salt sheet.

4.1. *Analogue materials and scaling*

The experiments are scaled with respect to different analogue materials according to their physical and mechanical properties. All are

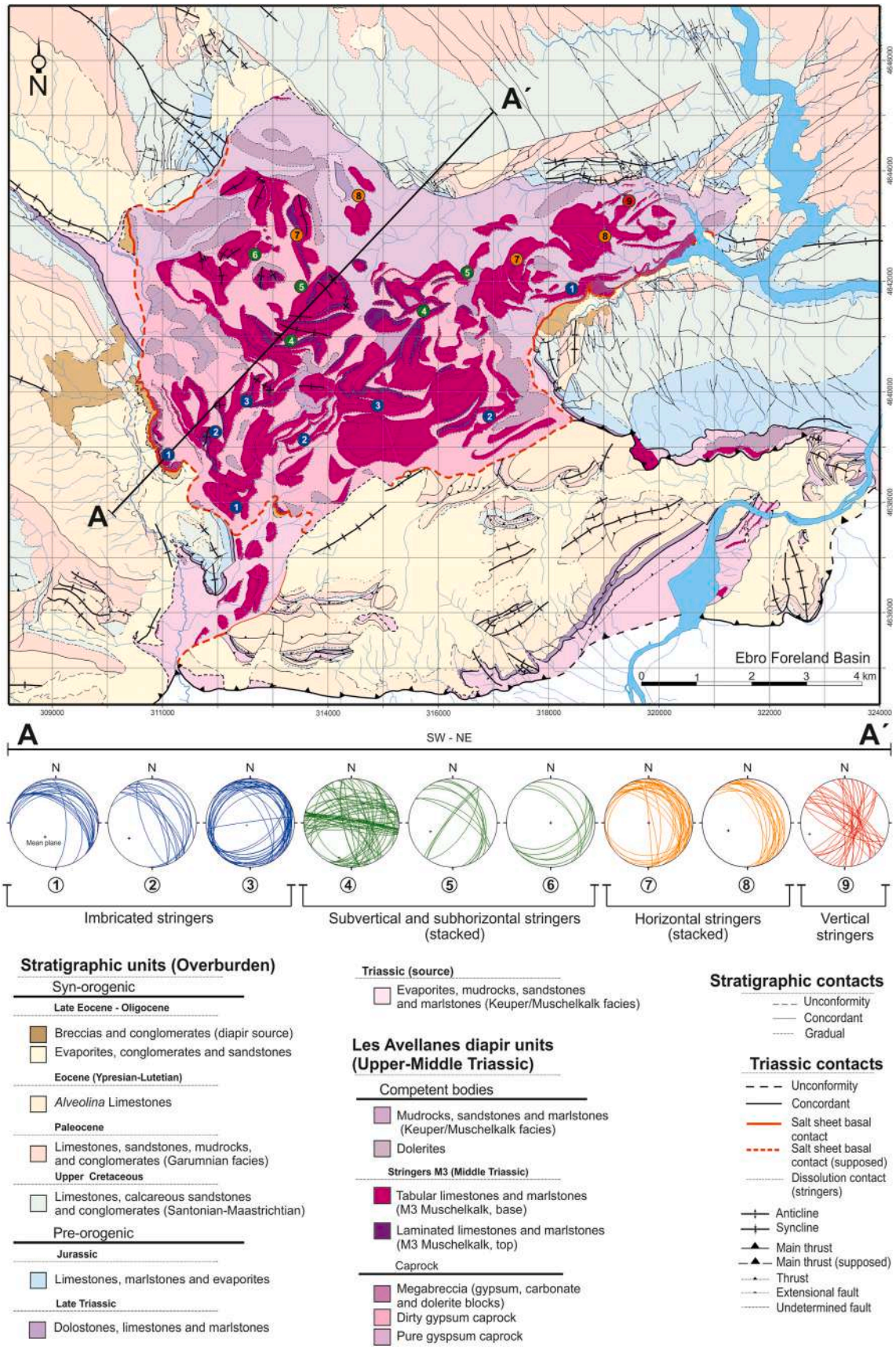

Fig. 7. Geological map of the *Les Avellanes* Diapir (1:5000 scale) showing the distribution and facies of M3 stringers within the diapir exposure. Bedding of the M3 stringers was measured systematically within the diapir and is shown in equal-area, lower hemisphere stereographic projections where each number represents a locality where data was collected. A-A′ refers to the section trace of Fig. 8.

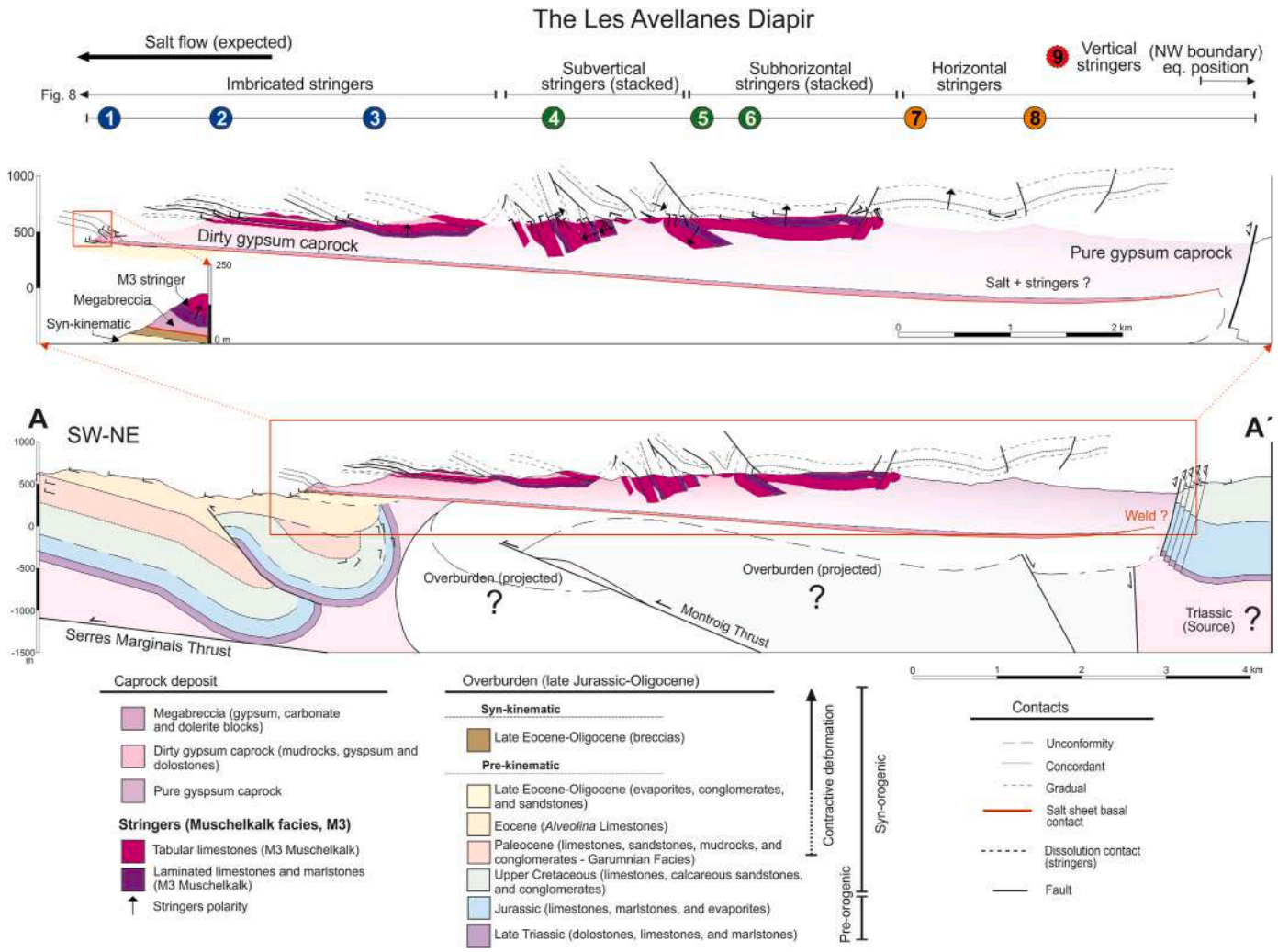

Fig. 8. Cross-section of the *Les Avellanes* Diapir. Numbers refer to the locations represented in Fig. 7. The section under the salt sheet has been projected considering the tectonic structures outcropping adjacently. The topographic information used to construct the cross-section was provided by the Institut Cartogràfic i Geològic de Catalunya (ICGC), HD-DEM, 2 × 2 m (MET-2) v2.0 (2016–2017) (https://icgc.cat), obtained from 2 m × 2 m resolution, filtered LiDAR data. Thicknesses of the adjacent units and stringers were obtained and projected combining the cartographical data with the high-resolution, LiDAR-based topography.

common analogues used in the physical modelling of salt tectonic structures (e.g. Bahroudi and Koyi, 2003; Dooley et al., 2005; Warsitzka et al., 2015, 2021a). The materials utilised for this experiment include: 1) silicone (polydimethylsiloxane, PDMS), used in S1 and S2 layers to simulate the viscous behaviour of salt, 2) granular, moderately well-rounded, coloured and uncoloured, dry quartz sand, to represent the overburden layers and the syn-shortening layers, 3) a granular mixture of sand and fillite, used for the intrasalt layer in order to reach the desired density of 1140 kg/m3 (Warsitzka et al., 2021b), and 4) glass beads, used to simulate the caprock matrix formed on top of the salt sheet by the continuous dissolution of the chlorides (Rosenau et al., 2022). The geometrical and mechanical material properties are summarised in Table 1.

To approach the dynamical similarity of the model to the *Les Avellanes* Diapir natural prototype, we followed a standard technique of scaling by comparing dimensionless ratios of velocities, geometry, and rheology between the model and nature prototype. Both prototype and model should also properly satisfy the Cauchy momentum equation governed by appropriate scaling (non-dimensional parameters) which reflects the interplay between the internal and external forces acting on the model (Weijermars and Schmeling, 1986). Thus, the model and the natural prototype should have the same (most similar) dimensionless dynamic parameters (e.g. Ramberg numbers, Stokes numbers, Reynolds numbers, etc.).

For the scaling analysis, we tested the Ramberg numbers given by relation for brittle layers (B):

$$R^{B}_{m(N)} = \frac{\rho_B \cdot g \cdot h_B}{\tau_C}$$

and by relation for ductile layers (D):

$$R^{D}_{m(N)} = \frac{\rho_D \cdot g \cdot h_D^2}{\eta \cdot V}$$

where ρ is the density of a layer with thickness h, g is the gravitational acceleration, τ_C is the cohesion, η is the viscosity and V is the bulk velocity. Thus, considering the ratio of models' (m) and prototypes' (N), the Ramberg numbers should be ideally close to 1 or in the first order around 1. Based on this scaling analysis (Table 1), we can conclude that the presented model is in good correspondence to natural prototypes with minor deviations for complex viscous segments. The suggested ranges of rock rheological properties and bulk behaviour also restore the most probable natural scenario of stringer exhumation.

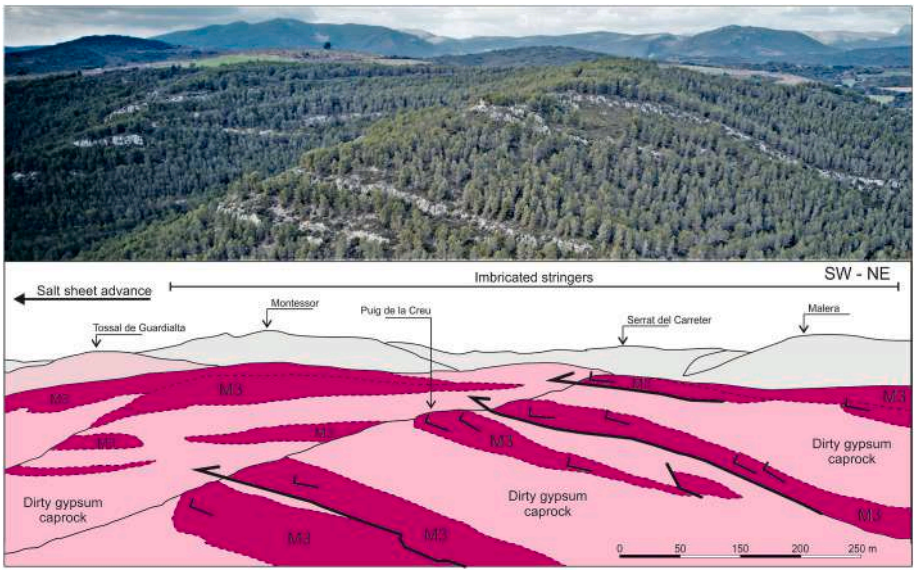

Fig. 9. DRON-collected aerial view of the South-central part of the *Les Avellanes* Diapir. An imbricated set of M3 stringers outcrops dipping northwards resembling a nappe structure.

Table 1
Scaling and mechanical parameters used in the experimental setup. Ranges are considered rather than exact values to reflect the uncertainty which is given by the unknown initial state of deformed rocks (e.g. porosity gradient, composition gradient etc.) or the spatial-temporal behaviour of various zones in a bulk. Thin and spatially restricted caprock is excluded from the global scaling analysis since it occurs only for a few selected stages of modelling and its geometrical restoration in a frame of deformed bulk is not straightforward. The bulk density of glass beads (model caprock) is noted below Table 1. For more specific rheological properties of the glass beads we refer to Rosenau et al. (2022).

General	Model	Nature	Scaling ratio
Minimum thickness (m)	0.055	~1100	$5.0{\cdot}10^{-5}$
Maximum thickness (m)	0.071	~1420	$5.0{\cdot}10^{-5}$
Length (longitudinal, N–S) (m)	0,5	$1.0{\cdot}10^{4}$	$5.0{\cdot}10^{-5}$
Width (lateral, E-W) (m)	0,5	$1.0{\cdot}10^{4}$	$5.0{\cdot}10^{-5}$
Slope (°)	1.8	1.8	1
Density (kg/m^3)	~1300	1200–2700	$1.35{\cdot}10^{0}$–$6.0{\cdot}10^{-1}$
Bulk velocity (m/s)	$8.33{\cdot}10^{-7}$	$1.75{\cdot}10^{-9}$	$4.76{\cdot}10^{2}$
Time (s)	$5.4{\cdot}10^{4}$	$1.57{\cdot}10^{14}$	$3.43{\cdot}10^{-10}$
Gravitational acceleration (m/s^2)	9.81	9.81	1
Segmented			
Overburden sediments			
Density (kg/m^3)	1610 (±30)	1200– (2400)–2700	$1.35{\cdot}10^{0}$–$6.0{\cdot}10^{-1}$
Thickness (m)	$2.0{\cdot}10^{-2}$–$3.6{\cdot}10^{-2}$	$4.06{\cdot}10^{2}$–$7.16{\cdot}10^{2}$	$4.92{\cdot}10^{-5}$–$5.02{\cdot}10^{-5}$
Coefficient of internal friction	$6.3{\cdot}10^{-1}$	$6.0{\cdot}10^{-1}$	$1.05{\cdot}10^{0}$
Cohesion strength (Pa)	$7.5{\cdot}10^{1}$	$3.0{\cdot}10^{7}$	$2.5{\cdot}10^{-6}$
Ramberg number	***6***	***0.44***	$\boldsymbol{1.3{\cdot}10^{1}}$
Intrasalt layer			
Density (kg/m^3)	1140	2300–2700	$5.0{\cdot}10^{-1}$–$4.2{\cdot}10^{-1}$
Thickness (m)	$1.00{\cdot}10^{-3}$	$4.00{\cdot}10^{2}$	$2.5{\cdot}10^{-5}$
Coefficient of internal friction	$6.5{\cdot}10^{-1}$	$6.3{\cdot}10^{-1}$	$1.0{\cdot}10^{0}$
Cohesion strength (Pa)*4	$7.0{\cdot}10^{1}$	$1.0{\cdot}10^{7}$–$5.0{\cdot}10^{7}$	$7.0{\cdot}10^{-6}$–$1.4{\cdot}10^{-6}$
Ramberg number	***0.16***	***0.18–0.90***	$\boldsymbol{0.9{\cdot}10^{-1}}$–$\boldsymbol{1.7{\cdot}10^{1}}$
Salt			
Density (kg/m^3)	970	2200	$4.4{\cdot}10^{-1}$
Thickness (m)	$3.7{\cdot}10^{-2}$	$6.6{\cdot}10^{2}$	$5.6{\cdot}10^{-5}$
Viscosity (Pa.s)	$2.2{\cdot}10^{4}$	$1.0{\cdot}10^{17}$–$5.0{\cdot}10^{18}$	$2.2{\cdot}10^{-13}$–$4.4{\cdot}10^{-15}$
Average compression rate (m/s)	$8.33{\cdot}10^{-7}$	$1.75{\cdot}10^{-9}$	$4.76{\cdot}10^{2}$
Ramberg number	$\boldsymbol{7.1{\cdot}10^{2}}$	$\boldsymbol{1.0{\cdot}10^{0}}$–$\boldsymbol{5.4{\cdot}10^{1}}$	$\boldsymbol{7.1{\cdot}10^{2}}$–$\boldsymbol{1.3{\cdot}10^{1}}$

* General values are taken from all the experiments (Segmented values correspond to the exp #4).
** Model materials were measured at the Institute of Geophysics (CAS in Prague) and GFZ (Potsdam).
*3 Nature values are averaged based on field observations and/or taken from Ge et al. (2019).
*4 For phi <0.3 (porosity) of carbonates (Ng and Santamarina, 2023).
*5 1 order difference between Rm and Rn are given by considering thicker multilayer for the prototype (thicker salt).
*6 Density of glass beads (the caprock) is 1585 ± 2 kg m^{-3} (Rosenau et al., 2022).

4.2. Model setup

The experiment was performed in a rectangular box (50 cm long, 50 cm wide) with a backstop wall (fixed wall) and an indenter (moving wall) attached to a programmable drive unit (Fig. 10A). The experimental stratigraphy was designed to approximate the field prototype

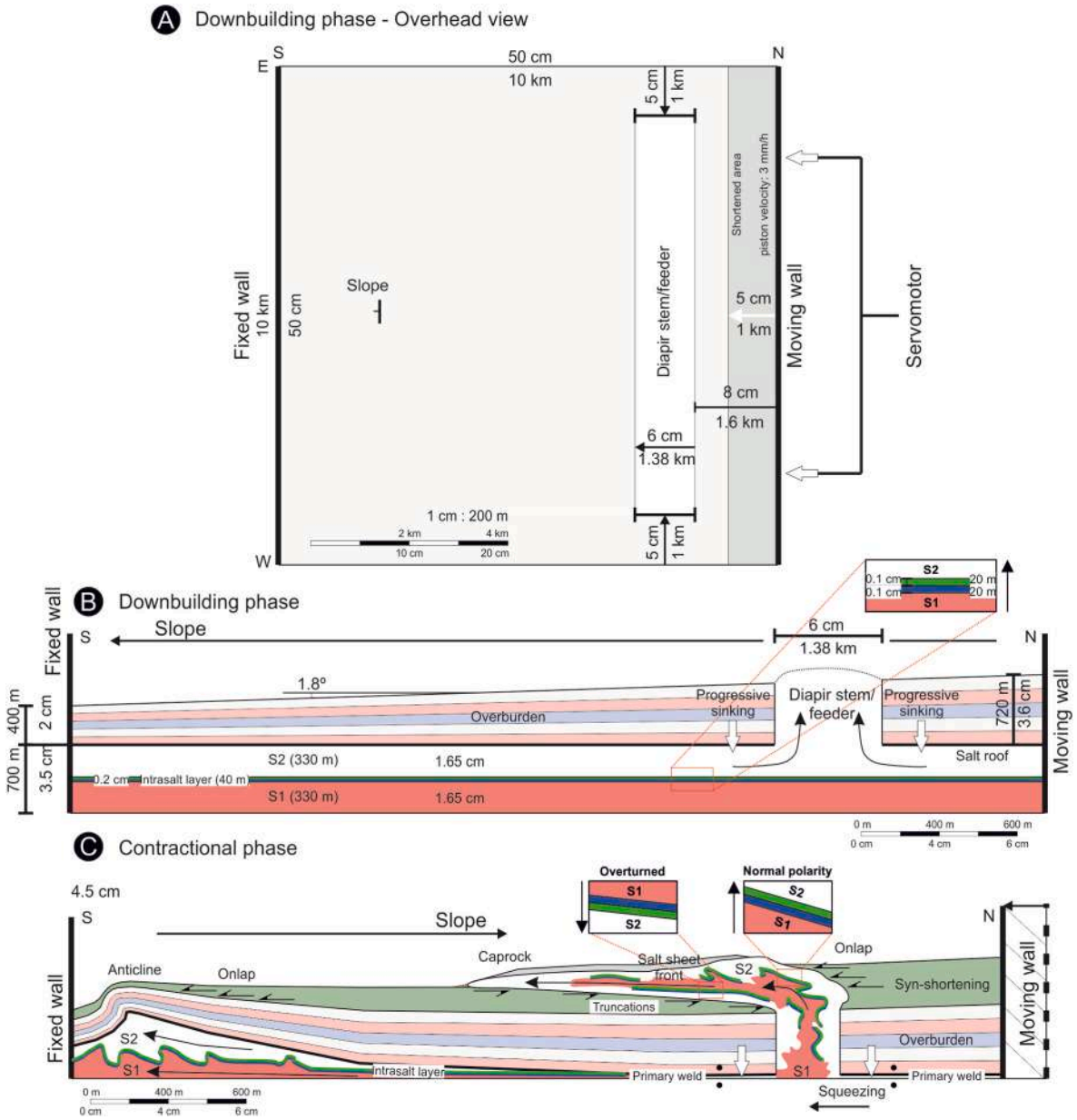

Fig. 10. Analogue model setup. North is oriented to the right. (A) Map view of the model. (B) Downbuilding phase, experimental stratigraphy before the active extrusion. (C) Contractional phase, experimental stratigraphy during and after the active extrusion.

with a focus on generating stringers during the diapir evolution. Since the model is naturally limited by the initial geometrical setup (buttressing effect), the stratigraphy is simplified and slightly deviates from the natural reference shown in Fig. 3. The model stratigraphy consists of two parallel silicone layers, 1.65 cm each (eq. to 330 m in nature), one tinted red at the bottom (S1) and one transparent on the top (S2) (Fig. 10B). These layers represent the two Triassic salt successions in the Pyrenees: the upper Muschelkalk (M2) and the lower to middle Keuper (K1 and K2) successions, respectively (Fig. 3). The Keuper K1 and K2 s are believed to be thicker than the Muschelkalk M2 (Salvany and Bastida, 2004; Calvet et al., 2004; Camara and Flinch, 2017). However, in the Pyrenees, the original depositional thickness of these units is unknown due to the intense deformation. Therefore, equal silicone layers were used to maximize the potential for stringers entrainment.

The two silicone layers were separated by a brittle, 2 mm-thick, sand layer that simulates the M3 Muschelkalk layer, and is named the intrasalt layer (Fig. 10B). In the reference sequence portrayed in Fig. 3, the M3 unit ranges from 20 to 80 m thick, so the value used in the model (2 mm of thickness, eq. to 40 m in nature) favours the expulsion of stringers formed by the fragmentation of this layer. The intrasalt layer is divided into two differently coloured intervals each 1 milimeter-thick, blue at the bottom and green at the top. This subdivision represents the main stratigraphical facies of the M3 stringers and allows the identification of their polarity (Fig. 3). On top of the S2 layer, a multilayer sequence composed of five sand layers, alternating red, blue and uncoloured sand, was deposited as the overburden. These layers are placed around a rectangular area with no deposited overburden that acts as a vertical (wall-shaped) conduit of the silicone.

In the model, the overburden layers represent the suprasalt, pre-orogenic to syn-orogenic sequence, ranging from the Late Triassic to the Eocene (Fig. 3). Overburden layers become progressively thicker towards the moving wall (3.6 cm, eq. to 720 m) and gradually wedge towards the fixed wall (2 cm, eq. to 400 m) with an overall slope of 1.8° (Fig. 10B). The thickness change is representative of the southward wedging of the overburden in the *Les Avellanes* Diapir area, changing from around 1200 m thick at the north to around 800 m thick at the

south (Cofrade et al., 2022). However, the overburden thickness in the model was reduced to avoid its rapid subsidence. The slope represents the orogenic wedge created during the Oligocene, which dips foreland-ward (Garcés et al., 2020).

On top of the overburden, syn-shortening layers (green coloured sand) are sieved during the extrusion of the silicone behind and in front of the spreading silicone body (Fig. 10C). This simulates the deposition of the late Eocene-early Oligocene units, covered by the allochthonous salt sheet.

4.3. Procedure

The general procedure can be divided into a downbuilding phase and a contractional phase where shortening was applied to the model. During the downbuilding phase (Fig. 10B), overburden layers were sieved on top of the silicone layer (S2) forcing its flow and ascension through the vertical conduit due to loading. When the silicone reached the surface, a new layer was sieved, so the silicone remained concealed within the conduit. In turn, the overburden adjacent to the diapir gradually sank, producing a primary weld surrounding the stem and isolating the diapir from the source layer. After the sedimentation of the overburden, the silicone was left to spread for 1 h, forming an elevated bulge-shaped summit on top of the conduit. To simulate salt dissolution near the surface and the subsequent formation of the caprock matrix, this topography was manually removed, and instead, glass beads (model caprock/carapace) were sieved on top of the extruded silicone.

Next, the contractional phase was simulated by applying shortening (Fig. 10C). This was achieved by a software-controlled, motor-driven worm screw attached to the moving wall. Shortening was applied at a constant rate of 3 mm/h for 15 h, reaching a total shortening of 45 mm (eq. to 900 m). This squeezed the diapir conduit and induced the longitudinal extrusion of the silicone (Table 1). Glass beads were systematically added at 2 h intervals on top of the extruded silicone and over the feeder simulating the caprock matrix/carapace growth in nature. The dissolution of the chlorides during the longitudinal extrusion was not considered. Syn-shortening deposition was also added during this phase at the same intervals as the model caprock, covering the overburden (Fig. 10C). When the velocity of the extrusion dropped significantly, the experiment was stopped. Then, the model was covered by post-kinematic sand and soaked with a gelling agent to preserve the final topography and to avoid further silicone flow. Finally, the model was sliced parallel to the shortening axis in vertical serial sections (1 cm thick).

4.4. Monitoring

The experiment was captured by two independent camera systems for further analysis. At first, a single camera (Canon EOS 1300D, 18Mpx, lens Canon EF-S 18–55 mm f3.5–5.6 IS II) was used for quick and direct overhead imaging. The same camera was later utilised to produce a sequence of images during the sectioning of the model.

To provide a detailed dynamical analysis of the overhead evolution, state-of-the-art strain monitoring methods were applied to derive quantitative deformation (strain) data from the model (e.g. Adam et al., 2005; Warsitzka et al., 2013, 2015, 2021a; Krýza et al., 2019, 2021, 2022). The model surface was monitored by a stereoscopic system of two digital 12-bit monochrome CCD cameras with a resolution of 29 megapixels (LaVision Imager M-lite 12 M) at a time interval of 120 s (0.01 Hz frequency). The recorded stereoscopic images were processed with DIC techniques performed by DaVis software (2D-/3D Stereo Digital Image Correlation, DaVis software), which provided surface topography together with the incremental surface 3D displacement field with high accuracy ($\leq$0.1 mm) (e.g. Adam et al., 2013; Warsitzka et al., 2013, 2021a). The model analysis was focused on a volumetric and isovolumetric part of the strain rate tensor. Thus, we derived the divergence of the velocity field and the shear strain rate that corresponds to extension/compression and horizontal movement along fault zones (Krýza et al., 2019, 2021). In our case, the strain analysis was applied in the model caprock on the salt sheet, since uncovered silicone is transparent for the analysis. In addition, spatial averaging of these parameters over selected model subdomains helped us to distinguish the prevalence of the respective deformation regime in various areas during model evolution. Calculations span for 2 h and 1 h intervals and are plotted in strain vs. time graphs to observe the variation of the strain regime, which is further supported by the structural evolution in the model.

4.5. Model results

4.5.1. Overhead strain pattern evolution

During the downbuilding phase, the salt analogue (silicone, from now on salt) ascended through the stem filling the diapir conduit at a pace equivalent to the sedimentation rate of the overburden layers (Fig. 11A and 12 A.1). Therefore, both divergence and shear strain rates over the stem remained positive and were increasing over time (Fig. 12A.2–A.3, Area 1).

Initially, the intrasalt layer, visible through the transparent S2, formed a symmetrical, vertical isoclinal anticline oriented parallel to the stem walls (Fig. 11A). This anticline was carried upwards by the ascent of salt, its hinge being subsequently stretched. Steeply inclined, tight to isoclinal folds were also present in the anticline limbs. At the end of the downbuilding phase, this anticline broke along its hinge splitting into two fragments. Steeply inclined folds were also stretched and dismembered within the stem creating stringers, which were also oriented parallel to the walls. These stringers were transported into the upper section of the stem and transposed to recumbent folds.

During the contractional phase, shortening squeezed the diapir stem and triggered the extrusive advance of an allochthonous salt sheet (Figs. 11B and 12B.1-B.2), which was moving initially downslope (Fig. 12B.1). Thus, the salt flow accelerated, spreading over the syn-shortening strata as the dynamic bulge above the stem collapsed asymmetrically downslope. Therefore, the stem acted as the feeder of the allochthonous extrusion (Figs. 11B and 12B.1). The slope of the overburden wedge (Fig. 10B) focused the salt advance direction southward resulting in an asymmetric salt sheet. After only 2 h of shortening (6 mm of squeezing), the salt sheet quickly covered an area approximately 6 cm wide (Fig. 11B). Accordingly, the divergence and shear strain rates attained maximum values during this phase. They were higher over the spreading salt sheet (Fig. 12B.2–B.3, Area 2) compared with the feeder (Fig. 12B.2–B.3, Area 1).

Model caprock deformation on top of the salt sheet was recorded in the overhead view by the development of extensional faults and minor folds. The areas directly on top of the feeder core remained mostly undeformed, although surrounding these areas, extensional faults continuously developed oriented in two E-W oriented belts, located North and South from the feeder (Figs. 11B and 12B). These faults dismembered the model caprock into rafts which glided over the sheet towards the sheet front. In addition, the horizontal flow out of the feeder carried the stringers into the advancing sheet, also moving towards the salt sheet front (Fig. 11B). Bounding the stringers' traces, extensional and compressional bands were also developed, gradually migrating toward the salt sheet front along with the stringers.

Localised divergence and shear strain further confirmed the observed deformation in the model caprock and was reflected by the development of extensional structures. Therefore, over the feeder, the surrounding extensional belts correspond to areas with high values of positive divergence and relatively high shear deformation rates. The undeformed areas on the feeder registered close to zero strain (Fig. 12B.2–B.3, Area 1). Local deformation within the salt sheet was mainly observed along E-W fringes matching the traces of the stringers. Negative divergence values were detected upstream from the traces of stringers, concordantly with the orientation of the compressional bands. Divergence maximums

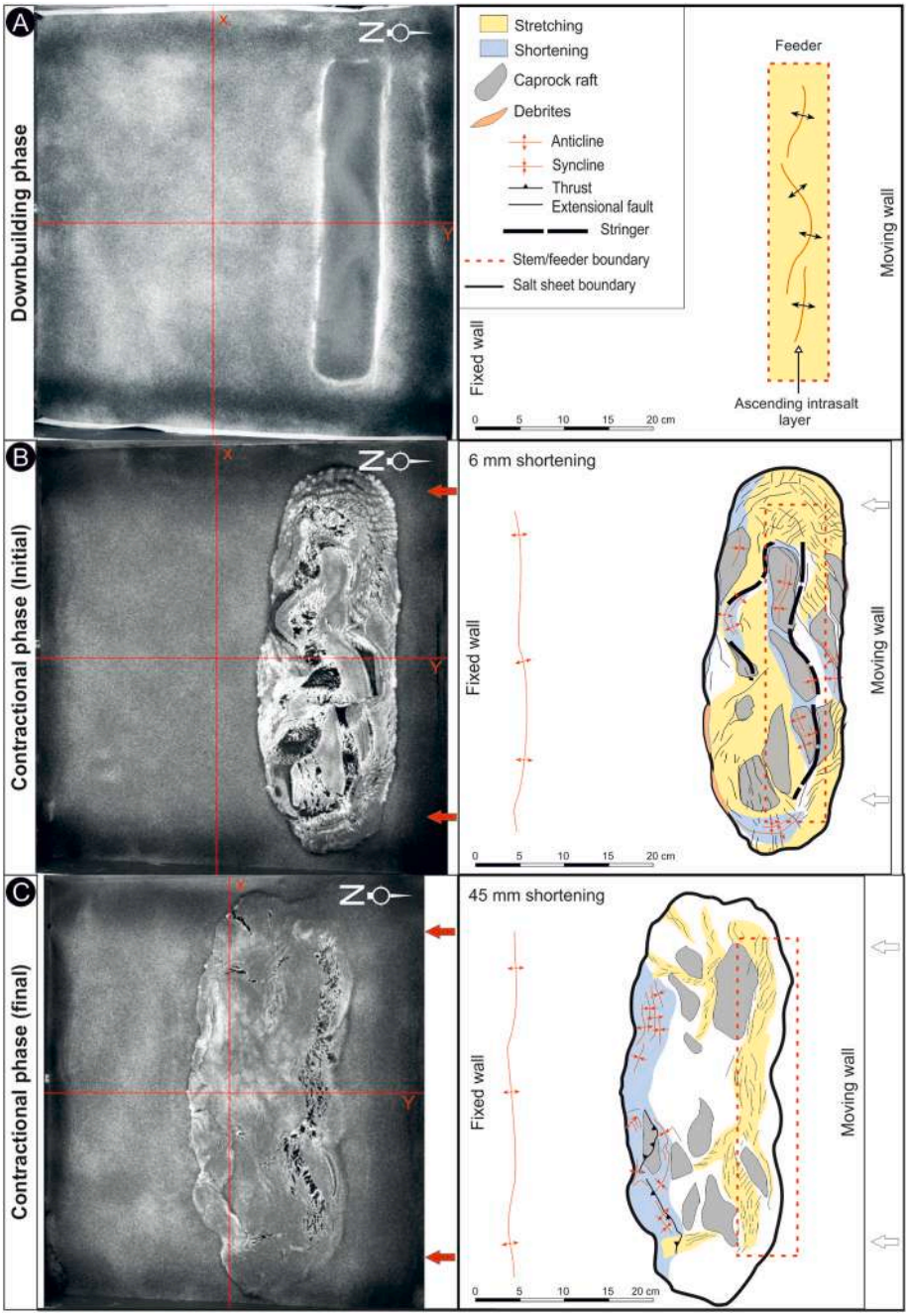

Fig. 11. Overhead pictures showing the evolution of the model and interpreted sketches. The areas where extensional and compressional structures were preferentially developed have been coloured. North is oriented to the right. (A) End of downbuilding phase after the deposition of the overburden sequence. (B) Contractional phase after 2 h of shortening (6 mm total shortening, eq. to 600 m in the nature prototype). (C) End of the contractional phase after 15 h of shortening (45 mm of total shortening, equivalent to 2600 m in the nature prototype).

were located downstream, where the rafts were stretched. Similarly, the higher shear strain values were also concentrated along the boundaries of stringers (Fig. 12B.2–C.2, Area 2).

As the syn-shortening layers were sieved northward from the feeder and southward from the salt sheet front, the transported caprock rafts and stringers accumulated and gradually disaggregated to form a debrite-like deposit at these lateral limits of the flow (Fig. 11B). As the salt sheet advanced upsection climbing on the syn-shortening sedimentary layers, these debrites were finally overridden by the advancing salt sheet.

Along the fixed wall, a detached anticline gradually developed by salt inflation (Figs. 11B and 12B). This anticline was nucleated during the downbuilding phase as salt flowed toward this area due to the gradual sinking of the overburden next to the diapir. The resulting salt bulge was subsequently amplified during the contractional phase as a consequence of the strong buttressing effect exerted by the fixed wall. Therefore, the development of this anticline changed the general slope orientation, so the salt sheet progressively advanced uphill during the contractional phase (Figs. 11C and 12C).

At the end of the contractional phase, the salt sheet gradually slowed down, finally covering an area 13 cm wide (Fig. 11C and 12C.2). Therefore, both shear strain and divergence trends approached zero during the end of this phase (Fig. 12B.3–C.3, Area 1 and Area 2). Surrounding the feeder, some areas of the model caprock still recorded

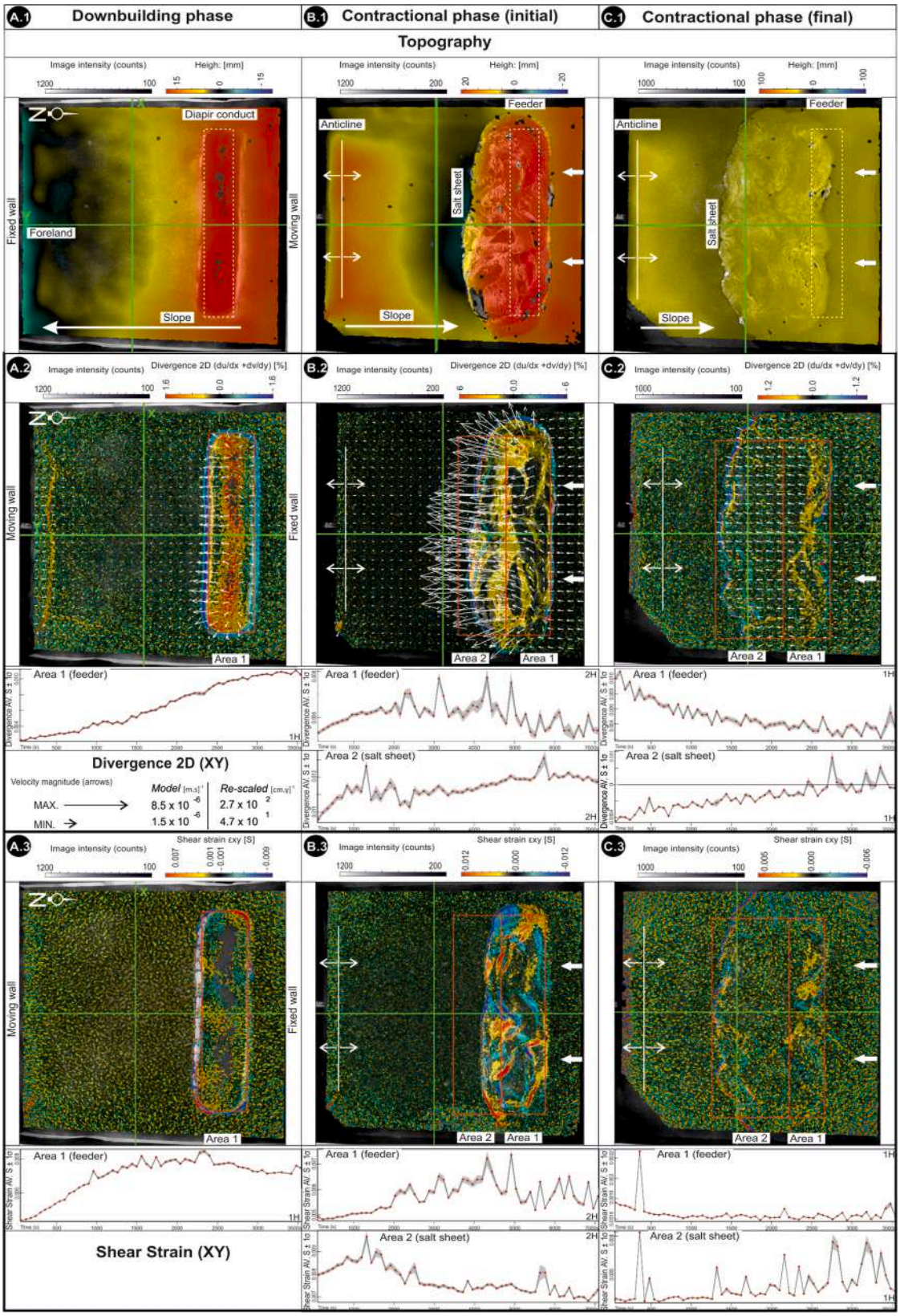

Fig. 12. Strain maps produced by the stereographic system of strain quantification (LaVision GmbH software). From top to bottom: 1) Topographic relief, 2) divergence and 3) shear strain rates, in overhead view. From left to right: (A) End of the downbuilding phase after the sedimentation of the model caprock (eq. to Fig. 11A). (B) Contractional phase after 2 h, 6 mm of total shortening (eq. to Fig. 11B). (C) End of the contractional phase after 15 h, and 45 mm of total shortening (eq. to Fig. 11C). Velocities (white arrows) in A.2, B.2 and C.2 are represented as scaled vectors (see factors plotted). Calculated strain divergence (2D) and shear strain components in Area 1 and 2 are plotted vs. time to complement each map. Area 1 corresponds to the feeder region and Area 2 corresponds to the salt sheet region (see red polygons for location). North is oriented to the right. (For interpretation of the references to colour in this figure legend, the reader is referred to the Web version of this article.)

extensional structures (Fig. 11C). However, in the salt sheet front, E-W belts of compressional structures developed and gradually propagated backward. In this frontal area of the salt sheet, small, millimeter-scale folds formed, and rafts were imbricated creating thrusts and back-thrust systems. Concordantly, negative divergence was detected in the sheet front, matching the area where compressional structures were localised. In addition, shear strain rates in the salt sheet area were above the values in the feeder area, reflecting the development of these compressional structures (Fig. 12B.3–C.3).

4.5.2. Cross-sectional architecture and stringer configuration

Cross-sections of the experiment show the 3D structural style at the end of the model evolution. The model salt structure was characterised by an asymmetrical salt sheet that advanced over the syn-shortening sedimentary layers (Fig. 13). We describe the internal architecture of the model first in the diapir stem and then in the salt sheet.

The core of the diapir stem and its base is occupied by the S1, while S2 is located near the walls and within the dynamic bulge over the stem (Fig. 13C). The salt over the northern flank of the diapir was progressively covered after the deposition of the third syn-shortening layer forming a north-dipping shoulder (Fig. 13A–B). The syn-shortening layers of this shoulder gradually thicken towards the diapir (Fig. 13A–C). Locally, this shoulder collapsed into the stem as extensional faults nucleated at cusps of the onlapping strata (Fig. 13B, section C2). In addition, primary welds developed below the overburden to the North and South from the stem as the salt escaped from the source layer toward the stem and into the allochthonous body (Fig. 13C). In consequence, while few stringers remained within the lower part of the diapir stem, most of them are found in the upper section, divided into two subvertical sets. Consecutive cross-sections of the model revealed that both sets of stringers are striking perpendicular to the shortening direction and rotated southward over the stem and over the southern flank of the diapir. The stringers located closer to the northern flank reached the top section of the feeder, where they form isoclinal and recumbent folds. The limbs of these folds are subhorizontally stacked and display alternating polarities (Fig. 13C, sections C1, and C3).

The allochthonous salt has a base dipping to the North, updip over cutoffs of the syn-shortening layers. The salt top is mostly subhorizontal

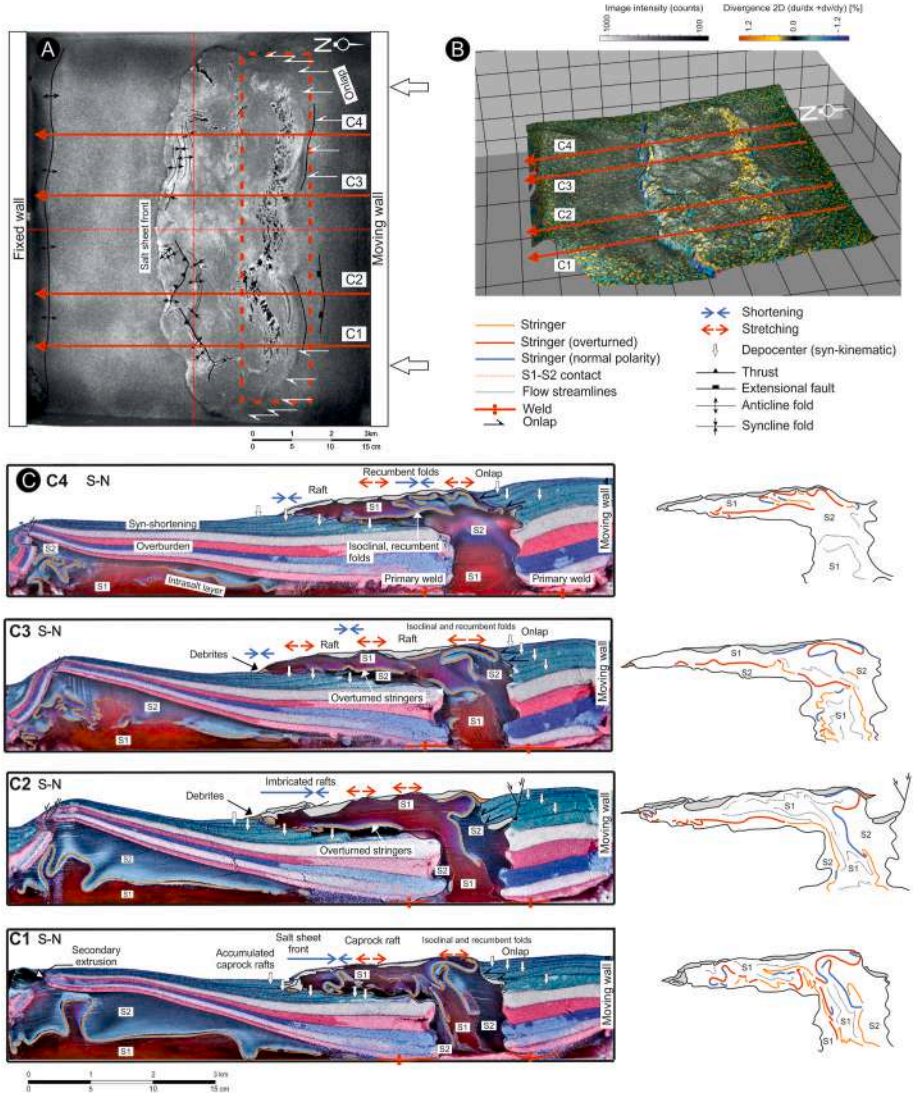

Fig. 13. (A) Overhead view of the model with interpreted structures at the end of the contractional phase. (B) 3D view of the model at the end of the contractional phase with 2D divergence to highlight the areas of stretching and shortening. (C) Interpreted cross-sections of the model at the end of the experiment and sketches of the diapir and salt sheet highlighting the structural style and the distribution of the stringers. Red and blue arrows represent stretching and shortening of the model caprock, respectively. Stringers in the sketches are coloured red or blue to represent their stratigraphical polarity. The location of the cross-sections is indicated in Fig. 13A and B. North is oriented to the right. (For interpretation of the references to colour in this figure legend, the reader is referred to the Web version of this article.)

and slightly dipping towards the salt sheet advance direction (Fig. 13C). The salt sheet displays an inverted stratigraphy with the S1 salt unit in the core and upper section of the salt sheet, and the S2 salt unit along the base (Fig. 13C). Stringers within the salt sheet are divided into two subparallel sets according to their position, one set located near the basal contact and the other closer to the salt sheet surface. These two sets of stringers reveal two different structural styles: 1) highly discontinuous stringers with gently inclined folds verging southward and recumbent folds close to the top of the salt sheet (Fig. 13C, sections C1, C3 and C4); and 2) rarely folded, more continuous overturned stringers parallel to the base of the salt sheet (Fig. 13C, sections C2 and C3). At the front of the salt sheet, discontinuous fragments of stringers are mostly dipping toward the frontal lobe and some of them are imbricated.

Toward the fixed wall shortening arched the detached anticline along this wall. This was coupled with a progressive extensional thinning of its crest, developing collapsed grabens. As shortening increased, small roof overthrusts developed at the front limb of the anticline. The salt also extruded locally, assisted by these faults. At the core of the anticline, the intrasalt layer is mostly continuous or affected by low-amplitude asymmetric folding.

5. Discussion

The experiment described above explored the extrusion of a stringer-bearing salt sequence, shedding light on the compartmentalization of the internal flow caused by the encased stringers. These stringers were folded and fragmented in consecutive steps during the salt sheet advance and finally, a few of them were imbricated when the sheet advance was decelerating. The model presented achieved: 1) the formation of stringers by the dismembering of the intrasalt layer; 2) the exhumation and folding of these stringers within the salt flow; 3) the development of a salt sheet; and 4) the deformation, migration, and accumulation of the stringers within the allochthonous body.

In this section, the experiment evolution is interpreted by relating the position, and the deformation style of the stringers with the horizontal salt flow. Then, the internal architecture of the *Les Avellanes* Diapir is discussed to evaluate the diapir geometry and to interpret its evolution from the configuration of the M3 stringers preserved in the evaporitic caprock matrix.

5.1. The internal structure of a diapir as a consequence of the salt flow

The structural configuration of the stringers and the model caprock deformation observed during the model evolution can be interpreted relative to the salt flow. These interpretations are supported by the strain maps (Fig. 12), portraying the role of the stringers within the internal deformation of an advancing salt sheet.

5.1.1. Internal structure during the downbuilding phase

As the intrasalt layer was gradually stretched (Figs. 11A and 12A), two sets of E-W oriented stringers formed within the stem. Natural examples show that verticalized stringers dominate near diapir boundaries and tend to line the diapir core where older layers are found (Hudson et al., 2017; Alsop et al., 2016), and thus, the model reproduced this configuration. The stringers over the diapir vent were refolded into isoclinal, recumbent folds (Fig. 13C, sections C1, C2, and C3). This geometry is explained by the gravitational collapse of the viscous flow, where the silicone (salt) started spreading over the vent of the diapir (Talbot and Jackson, 1987; Talbot et al., 1999; Jackson and Hudec, 2017b). As the hinges of the folded stringers were gradually closed by vertical shortening and horizontal spreading of the host salt, the fold pattern formed horizontal stack-like configurations with alternating polarities.

5.1.2. Internal structure during the contractional phase

The rapid allochthonous advance at the beginning of the contractional phase was mainly sustained by shortening, which caused an enhanced salt supply rate since salt was continuously expelled from the feeder due to the squeezing of the diapir conduit. In nature, allochthonous emplacements occur when the salt supply rate exceeds the local sedimentation rate (McGuiness et al., 1993; Koyi, 1998). The sum of sedimentary loading and tectonic shortening results in an enhanced salt flow toward the surface, which may form allochthonous bodies locally, even if they are covered by a strong roof (Dooley et al., 2015; Duffy et al., 2018; Peel et al., 2020; Cofrade et al., 2023a).

During the allochthonous salt advance initiation, the diapir structure rotated southward, S2 occupied the core of the salt sheet, while S1 was near its top and bottom surfaces (Fig. 13C). Accordingly, the vertical stringers within the stem rotated as they entered the allochthonous body, lining the core of the salt sheet. The uneven deformation between the top and the bottom sets of the stringers can be related with the Couette flow profile within the salt sheet (Talbot and Pohjola, 2009; Pichel et al., 2019). Therefore, faster flow near the surface of the salt sheet probably favoured the deformation of the stringers in the upper set (Fig. 13C, sections C2, C3, and C4). On the contrary, slower flow near the base of the sheet induced a smaller degree of deformation in the bottom set of the stringers, which were more continuous and rarely reached the frontal portion of the flow (Fig. 13C, sections C2, C3, and C4).

The deformation of the model caprock was controlled by the kinematics of the underlaying horizontal flow of the salt. This is reflected by the type and distribution of the structures developed during the model evolution, and by the location of the strain (Figs. 11 and 12). The model caprock overlying the dynamic bulge above the feeder was not intensely deformed. This is linked to a small degree of lateral diffluence, where the flow transforms from vertical to horizontal (Buisson and Merle, 2002, 2004). (Fig. 12B.2). Within the salt sheet, the deformation of the model caprock was mainly concentrated along the surfacing stringers (Fig. 12B.2–B.3). Strain variation registered over the salt sheet was controlled by the compartmentalization of the flow induced by the folded stringers. The stringers transported inside the salt sheet behaved as transient obstacles forming levee-style embankments that locally concealed the horizontal flow, thus changing the flow velocity profile. Thus, the deceleration of the flow immediately upstream from the stringers produced the compression linked with the thrusting and folding of the model caprock, and the acceleration downstream produced the stretching associated with caprock fragmentation. This process was similar to how salt-sediment interface irregularities induce deformation in brittle layers on top of flowing salt (Dooley et al., 2017; de Oliveira Santos et al., 2023). Additionally, as the flow carried the stringers toward the salt sheet front, the belts of local contraction and extension in the model caprock simply migrated downstream (Fig. 11B). The embankment effect was temporary and eventually the salt overflowed some of the surfacing stringers, which sank into the salt sheet. Therefore, the deformation of the model caprock was dynamically changing with respect to the configuration of the stringers during the salt sheet advance.

At the end of the contractional phase, the advance of the salt sheet was progressively hindered due to the change of the topographic slope produced by the inflation of the anticline along the fixed wall, and the accumulation of syn-shortening layers in the foreland of the extrusion (Fig. 13A). The decelerating advance was manifested in the general reduction of the divergence and the shear strain values in both the feeder and salt sheet areas (Fig. 12C). In consequence, the salt sheet body thickened and compressional structures (folds and thrusts) developed in the model caprock at the salt sheet front (Fig. 11C). This is compatible with negative values of divergence in this domain. Therefore, at the end of the model evolution, the salt sheet was divided between two distinctive zones perpendicular to the shortening direction (E-W), located over the feeder and in the salt sheet front, respectively. Extension prevailed over the feeder and shortening along the salt sheet front. In salt glaciers, the destabilisation of the caprock caused by the

diffluence of the flow over the feeder results in the development of extensional faults, which stretches the caprock and dismembers it into rafts that glide toward the advancing lobe (Yin and Groshong, 2007; Závada et al., 2021). Whereas extensional structures prevail in the feeder domain, the frontal parts of a salt glacier are usually characterised by concentric folds and faults (Talbot et al., 1999; Cosgrove et al., 2009; Talbot and Pohjola, 2009; Frumkin et al., 2021; Santolaria et al., 2021; Závada et al., 2021). Concentric folding may be formed as gliding caprock from the feeder slumps and accumulates at the leading edge of the flow (Jackson and Hudec, 2017b; Závada et al., 2021). In addition, the inhibition of the salt sheet advance may be also caused by progressive dissolution from the leading edge upstream (towards the core) of the salt flow.

5.2. *Understanding the architecture of the Les Avellanes Diapir based on modelling results*

The assemblage of the M3 stringers observed in the *Les Avellanes* Diapir present three distinctive structural domains distributed coherently along the diapir geometry (northern, central and southern domains) that are compared with the model (Figs. 7–9). In the northern domain, just a few stringers are exposed and they are widely separated (Fig. 14A.1). Additionally, in the NW and NE corners, some subvertical M3 stringers are oriented parallel to the stem wall and slightly southward, these M3 stringers adopt a subhorizontal configuration (Fig. 14B). In the model, the stringers in the feeder formed isoclinal and recumbent folds, with the limbs piled up vertically changing from vertical to horizontal (Fig. 14C). The vertical configuration and the separation of the M3 stringers in the northern boundary of the *Les Avellanes* Diapir are in agreement with a feeder domain, which is interpreted along the northern boundary of the diapir (Fig. 14A.2). This interpretation is further supported by the salt sheet southward sense of advance (Cofrade et al., 2023a). Within the central part of the diapir, most of the exposed M3 stringers are accumulated (Fig. 14A.1). Here, the array of M3 stringers is characterised by juxtaposed subvertical and subhorizonal sets of stacked stringers with alternating polarities (Fig. 14B). Some of the M3 stringers are folded, compatible with the style of recumbent folds, and some are verging towards the advance direction (Fig. 14C). This is compatible with the salt sheet domain where horizontal flow dominates (Fig. 14A.2). In the southern domain of the diapir, the M3 stringers adopt a configuration that resembles a tectonically imbricated structure (Fig. 9). In the last stage of the model evolution, shortening was also observed in the model caprock of salt sheet front and some stringers were imbricated (Fig. 14C). The imbricated pattern of the M3 stringers

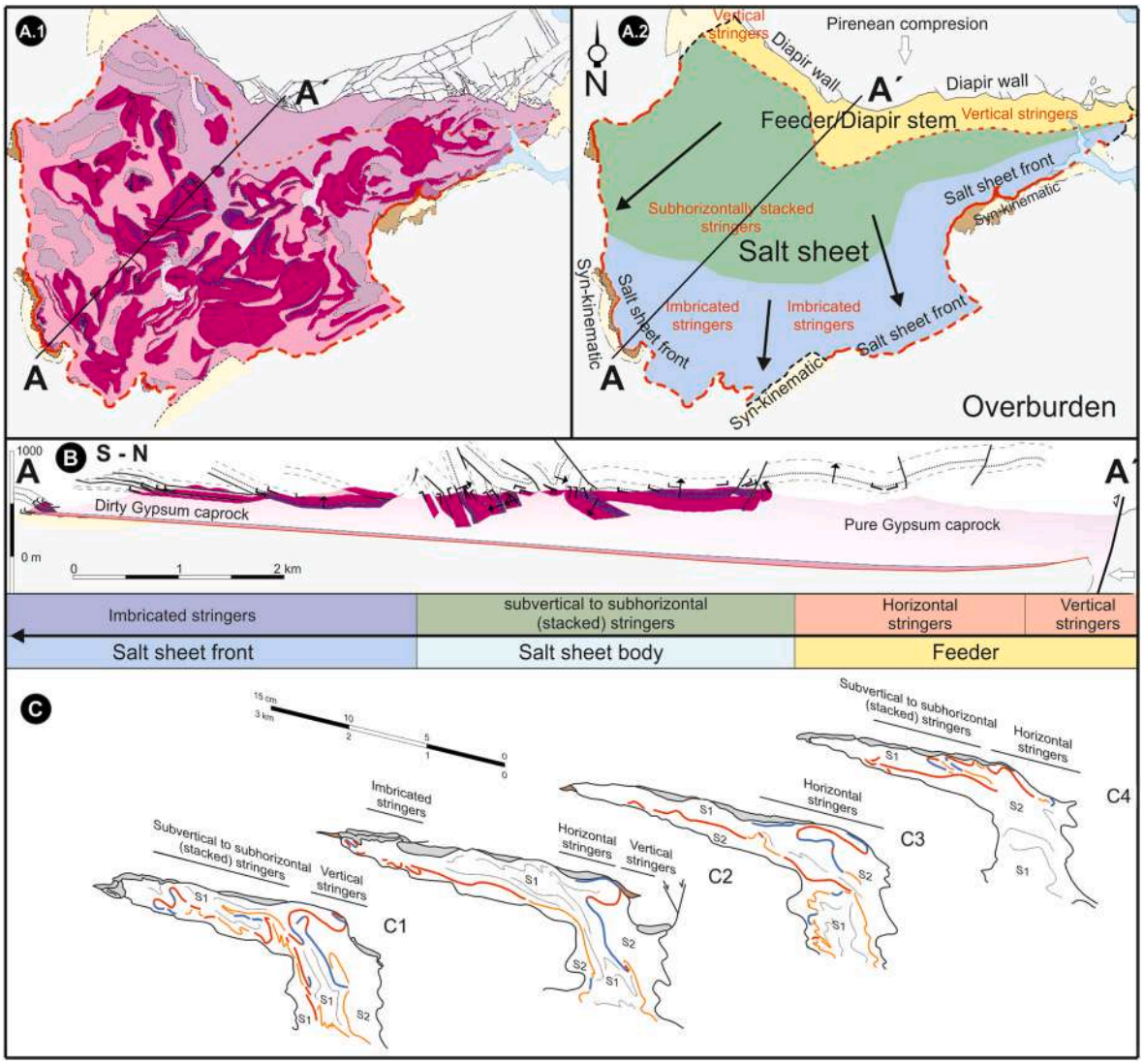

Fig. 14. (A.1) Simplified map of the interior of the *Les Avellanes* Diapir. Legend is located in Fig. 7. The trace of the cross-section in B is indicated. (A.2) Interpreted map of the *Les Avellanes* Diapir regarding the structural configuration of the M3 stringers. (B) Cross-section from Fig. 8 with the interpreted areas according to the configuration of the stringers. (C) Interpreted cross-sections (sketches) from Fig. 13.

along the southern boundary of the *Les Avellanes* Diapir suggest that the caprock was shortened, so the southern area of the *Les Avellanes* Diapir is interpreted as the salt sheet front domain (Fig. 14A.2). Moreover, the location of this domain is also supported by the stratigraphical relationships between the diapir and the late Eocene-early Oligocene host sequence (Cofrade et al., 2023a). Therefore, although the structural configuration of the M3 stringers in both the model and the *Les Avellanes* Diapir present variability and complexity, the northern, central and southern domains in the *Les Avellanes* Diapir are associated with the feeder, salt sheet and salt sheet front domains respectively, thus revealing the diapir geometry.

5.2.1. *The configuration of the stringers in the Les Avellanes Diapir and the diapir evolution*

Both the model and the *Les Avellanes* Diapir share similarities that can serve to interpret the evolution of the viscous flow within the advance of the salt sheet. Prior to the development of the allochthonous sheet, the Triassic LES was already exposed at the surface in the northern boundary of the diapir body, where a wall-shaped diapir was located. As observed in the model, fragments of the M3 stringers were ascending vertically in the diapir stem along two main paths striking parallel to the walls, thus lining the core of this diapir which was probably occupied by the M2 salt interval. As the M3 stringers were transported near the surface, they probably formed tight recumbent folds due to the vertical shortening and horizontal flow over the vent of the stem (Fig. 15A). This configuration was also observed by Hudson et al. (2017) in the Onion Creek Diapir where similar stringers, in both size and nature, were preferentially exposed along the diapir boundaries, whereas the core was dominated by a gypsum-rich caprock matrix.

The orogenic shortening continuously squeezed the vertical stem, promoting the allochthonous extrusion of the salt, so the core-to-wall zoning in the stem rotated as it entered the salt sheet. (Fig. 15B). The stringers were transported within the salt stem and expelled from the feeder separated in two main sets. The stringers currently exposed near the diapir surface were probably carried near the top surface of the salt sheet. The upper set of stringers adopted a subhorizontal configuration over the feeder domain as salt started to spread downhill. When entering into the salt sheet domain, these gently dipping folds preferentially rotated toward the advance direction, thus verging southward. These folded stringers were disrupted as the flow stretched the folds, which

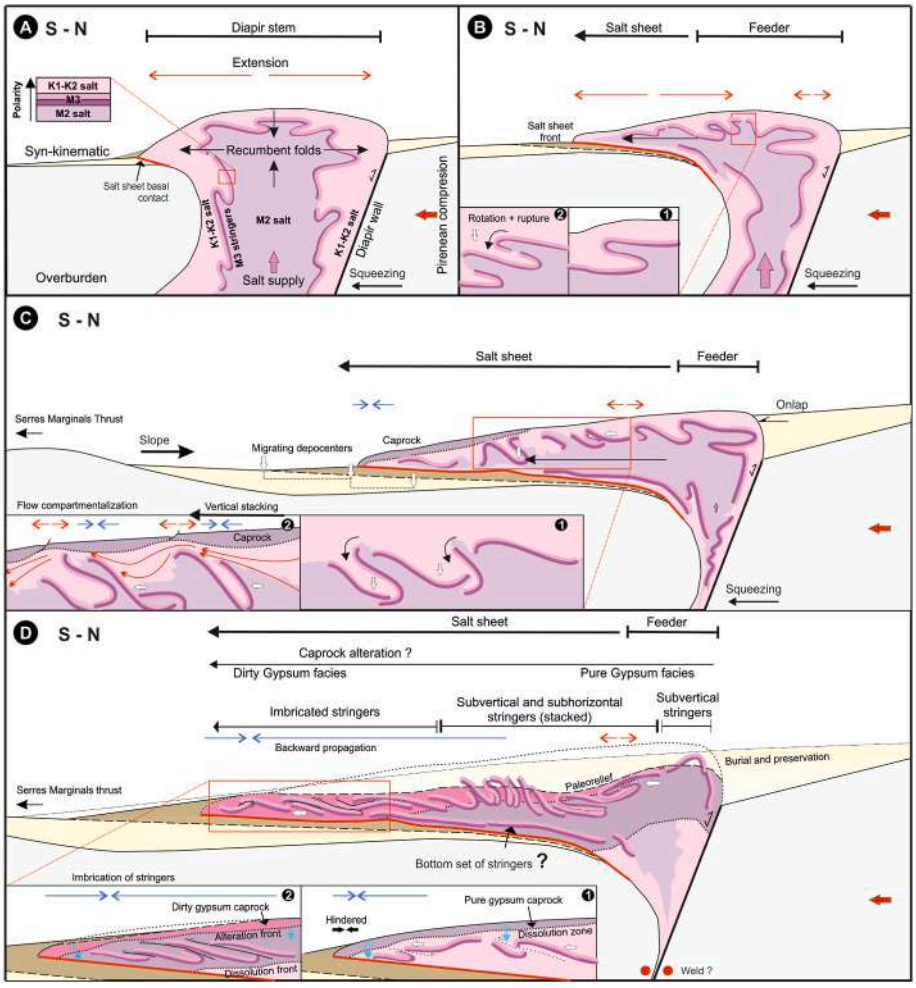

Fig. 15. Conceptual sketch showing the interpreted evolution of the *Les Avellanes* Diapir during the late Eocene-early Oligocene. North is oriented to the right. (A) Initial stage. Previously to the allochthonous salt extrusion, the gravitational collapse of the dynamical bulge over the diapir vent folds the M3 stringers intorecumbent folds, their limbs alternating polarities. (B) Early salt sheet stage. Stringers are transported toward the spreading salt sheet. 1–2 The stringers are rotated and broken as the host salt is advancing southwards. (C) Intermediate salt sheet stage and gradually decelerating salt flow advance. 1–2 Rotated folds are further fragmented along their hinge zones into individual limb-long stringers, the upper limbs overriding the lower limbs. Upturned stringers block the salt flow inducing compression and stretching upstream and downstream, respectively. At each such obstacle, longitudinally oriented stringers compartmentalise the horizontal flow. Stringers approach each other and stack together. (D) Salt sheet final stage. Minimum advance. 1–2 The caprock matrix starts accumulating preferentially along the salt sheet front. The hindering of the salt sheet front induces backwards propagating compression, so the stringers embedded in the caprock matrix are imbricated. The caprock matrix gradually thickens embedding the stringers array.

became fragmented. Some folds were broken preferentially along the hinges (Fig. 15B). As seen in model sections (Figs. 13C and 14C), another set of stringers may remain in the subsurface, carried near the base of the salt sheet.

During the salt sheet advance, the horizontal flow piled up these rotated fragments of the stringers, forming juxtaposed stacks of subhorizontal to subvertical stringers. The stack-like accumulations of stringers that appear in the salt sheet domain in the *Les Avellanes* Diapir are interpreted as the stacked limbs of these folded stringers. In addition, as observed in the model, these stacks of stringers probably created embankments that modified the flow within the salt sheet, concentrating the deformation along the stringer's margins (Fig. 15C).

As the ongoing shortening probably welded the diapir stem, the allochthonous advance in the *Les Avellanes* Diapir progressively decelerated. The welding of the stem is supported by the Oligocene conglomerates that postdate the northwest diapir boundary (Cofrade et al., 2023b). In addition to the welding of the stem and the corresponding decrease in salt supply the advance was hindered since: 1) the salt gradually dissolved inhibiting the flow, 2) the syn-shortening sedimentation increased in thickness southwards, overlapping parts of the salt sheet front; and 3) the regional slope changed during the emplacement of the Serres Marginals Thrust Sheet (Teixell and Muñoz, 2000; Cofrade et al., 2023a). As seen in the model, the consequence of the decelerating flow is the shortening of the caprock matrix located in the frontal parts of the salt sheet. The imbrication of the stringers at the salt sheet front domain in the *Les Avellanes* Diapir may suggest that these stringers were already embedded within the growing caprock matrix. In addition, the M3 stringers in this frontal location were mostly subhorizontally oriented, so the shortening of the caprock produced the imbrication of the stringers along the salt sheet front (Fig. 15D).

5.2.2. *Preservation of the stringers array*

Since the array of M3 stringers in the *Les Avellanes* Diapir mostly matches the configuration reproduced in the model, and the M3 stringers and the caprock matrix are not significantly disturbed (brecciated or fragmented), we can assume that the stringers array was preserved after the emplacement of the salt sheet (Figs. 7 and 14A.1). The preservation of the stringers array was probably caused by the growth of the evaporitic caprock matrix that encloses these stringers.

The growth of the caprock matrix probably was continuous during salt sheet advance as the emplacement occurred in a subaerial environment, which favours the progressive dissolution of salt. This suggests that during the salt sheet advance, a balance was established between salt supply and salt dissolution. This balance allowed for both, a continuous advance of the salt sheet, and the deformation of the M3 stringers within the salt flow. However, in salt glaciers, the proportion of salt decreases in the frontal part relative to the feeder, whereas the caprock proportion increases (Závada et al., 2021, 2023). Thus, in a similar fashion, the caprock thickness in the *Les Avellanes* Diapir was probably inhomogeneous during salt sheet advance.

The distribution of the two main caprock facies described along the *Les Avellanes* Diapir exposure (pure gypsum caprock and dirty gypsum caprock) may reflect the proposed inhomogeneous growth of the caprock. The pure gypsum caprock outcrops along the feeder area (northern area of the *Les Avellanes* Diapir), while the dirty gypsum caprock covers the central and southern areas of the diapir, where the salt sheet is located (Figs. 7, 8 and 15). Therefore, the presence of mudrocks and carbonates mixed within the gypsum gradually increases toward the salt sheet front. Besides, in the salt sheet front, carbonate breccias with abundant moldic porosity (Fig. 6F) and gypsum crystals partially replaced by carbonates (Fig. 6D) are also observed. These observations agree with a higher degree of alteration at the frontal part of the salt sheet. In addition, within the dirty gypsum caprock, some gypsum crystals are partially replaced by carbonates (Fig. 6D).

Therefore, the observed replacement process in the dirty gypsum facies also supports the suggested alteration trend. Since the gypsum that forms the caprock matrix is also significantly altered in subaerial conditions, the interpreted transformation trend in the *Les Avellanes Diapir* can be associated with the growth of an early and thus, thicker caprock along the salt sheet frontal domain. Moreover, due to the salt flow deceleration occurring during the final phase of the model evolution, the caprock along the frontal lobe of the salt sheet was shortened, and some rafts were imbricated here. Therefore, if the M3 stringers were already embedded in the thicker caprock matrix along the salt sheet frontal domain, the shortening of this part of the caprock may also explain the observed imbrication of the M3 stringers in this domain. However, the distribution of the caprock matrix facies could also reflect depositional variations in the proportion of mudrock, carbonate, and sulphate beds relative to the salt in the Triassic LES. Specifically, well logs penetrating the undeformed Triassic LES beneath the Ebro Foreland Basin tend to show an increase in mudrock and carbonate interbeds towards the stratigraphical top of the upper Keuper salt interval, equivalent to the K2 salt in the Pyrenees (Jurado, 1990). Assuming that the stratigraphy in the Pyrenean basin does not significantly change, as the Triassic LES mobilizes and deforms during the diapir and salt sheet stages, the upper and dirtier salt in the Triassic LES interval is more prompted to be located in the frontal lobe of the salt sheet. Accordingly, the increasing proportion of mudrocks within the frontal parts of the *Les Avellanes* Diapir can reflect this dirty salt interval at the top section of the Triassic LES, and not a stronger alteration of an early formed, thicker caprock. Thus, further investigation regarding the diagenesis of this caprock and the original stratigraphy of the Triassic LES is required to fully constrain this hypothesis.

Finally, as the stem was welded, the salt supply decreased so the balance between the salt supply vs the salt dissolution was disturbed. Therefore, after the advance of the salt sheet the caprock matrix growth rate increased. The rest of the caprock matrix grew rapidly as salt dissolved top-to-down, so the M3 stringers array was finally immobilised and preserved. However, the M3 stringers array may became further compacted as salt dissolved completely, without significantly changing its deformation (i.e. folded stringers cannot be refold by this mechanism). Finally, the salt sheet was buried by the Oligocene strata, postdating the salt extrusion, and contributing to the preservation of the stringers array.

6. Conclusions

The array of thick, carbonate M3 stringers within the interior of the *Les Avellanes* Diapir was reproduced using analogue models to understand the structural evolution of these stringers. The model allowed us to understand the evolution of the strain during diapirism in order to characterise the internal structure of this diapir. In this regard, the stringers array shows several characteristic configurations depending on the dynamics of the flow, which varied along the diapir geometry.

In the feeder domain, the stringers are vertically oriented, striking parallel to the walls of the stem. Toward the salt sheet domain, the stringers mainly adopt a subhorizontal position creating a characteristic array of recumbent and horizontally oriented folds. This configuration resulted as stringers reached the uppermost part of the stem, where the flow diverged and spread horizontally. The model caprock on top was stretched along two E-W oriented bands that surround an area of low deformation over the core of the feeder. The diffluence of the flow induced this deformation as the salt accelerated overflowing the stem walls.

During the allochthonous advance, the stringers were transported within the salt sheet aligned in two sets, one near the surface and the other near the base of the salt sheet. These two sets of stringers reflected the bulk rotation of the diapir zoning, which occurred during the initiation of the allochthonous advance. The Couette flow profile across the allochthonous extrusion with higher flow velocities at the top of the extrusion explains that the stringers closer to the surface were more fragmented and deformed than the stringers carried along the base,

which were more continuous and showed less deformation. In this regard, the upper array of stringers formed recumbent and gently inclined folds verging toward the direction of advance. These folds were broken within the advancing flow and rotating, so their limbs were subsequently imbricated, creating stacks of subvertical and overturned to subhorizontal stringers.

In addition, the strain measured on the surface of the model was concentrated along the trace of the surfacing stringers. These stringers concealed the horizontal flow forming levee-style embankments, comparable with the effect of base-salt irregularities. Thus, the salt decelerated upstream and then accelerated downstream from these docked stringers, registering alternating bands of compression and extension in the model caprock. These bands migrated from the feeder toward the sheet along with the stringers, so the deformation of the model caprock evolved with time.

As salt supply dropped, the advance of the salt sheet was hindered, and the flow decelerated. At the frontal lobe of the sheet, the decelerating flow induced the development of compressional structures in the model caprock (folds and thrusts), which gradually propagated backward from the frontal lobe.

The preservation of the stringer array in the *Les Avellanes* Diapir was possible since the large and competent M3 stringers were trapped in a rapidly growing caprock matrix, which probably started to form when the salt advance was terminated. Finally, the caprock matrix completely embedded the stringers and then was buried below synorogenic sediments, further preserving the studied array from intense mechanical alterations. Therefore, the *Les Avellanes* Diapir exemplifies a field approach to understand the diapir internal architecture based on the array of competent stringers. These stringers adopted a configuration produced by the salt flow, which supports the inferred geometry of the diapir and enables further understanding of the diapir evolution. In this regard, the *Les Avellanes* Diapir is proposed as an excellent analogue to investigate the internal deformation of an allochthonous salt body.

Declaration of competing interest

The authors declare that they have no known competing financial interests or personal relationships that could have appeared to influence the work reported in this paper.

Data availability

Data will be made available on request.

Acknowledgments

This work was supported by the Czech Science Foundation project No. 20–18647 J, and the Spanish projects: *SABREM* (PID2020-117598GB-C21), *SALTCONBELT* (CGL2017-85532-P), and DGICYT (PID2021-122467NB-C22) funded by Ministerio de Ciencia, Innovación y Universidades/Agencia Estatal de Investigación/Fondo Europeo de Desarrollo Regional, Unión Europea, the Grups de Recerca reconeguts per la Generalitat de Catalunya (Spain), 2021SGR349 “Geologia Sedimentària” and 2021SGR76 “Geodinàmica i Anàlisi de Conques”. GC also acknowledges the support of the UB scholarship PREDOC-UB19/20 5660400. We also acknowledge Paradigm (AspenTech) and Petroleum Experts (Petex) for providing the academic licenses of GoCad and Move software, respectively, used in field data collection, analysis and cross-section construction. The experimental part of this work was covered by the Tectonic Modelling Laboratory at the Institute of Geophysics of the CAS (Czech Republic). We also thank to Dr. Carl Fiduk, Dr. Tim Dooley, and Dr. Mark Rowan as referees for their very constructive reviews.

This paper is dedicated to the memory of our colleague and friend, Victoriano Pineda González. Victoriano was born in Almoradí (Alicante Province of Spain) on August 5, 1993, and died on March 9, 2023, at an underground potash mine in Súria, Barcelona. His death happened when Victoriano was nearing the end of his PhD studies. The incident occurred as a fragment of an intrasalt layer collapsed and trapped him within the gallery. May the knowledge of these layers help to prevent these fatal accidents in the future.

References

Adam, J., Klinkmüller, M., Schreurs, G., Wieneke, B., 2013. Quantitative 3D strain analysis in analogue experiments simulating tectonic deformation: integration of X-ray computed tomography and digital volume Correlation Techniques. J. Struct. Geol. 55, 127–149. https://doi.org/10.1016/j.jsg.2013.07.011.

Adam, J., Urai, J.L., Wieneke, B., Oncken, O., Pfeiffer, K., Kukowski, N., et al., 2005. Shear localisation and strain distribution during tectonic faulting: new insights from granular-flow experiments and high-resolution optical image correlation techniques. J. Struct. Geol. 27 (2), 283–301.

Al-Siyabi, H.A., 2005. Exploration history of the Ara intrasalt carbonate stringers in the South Oman Salt Basin. GeoArabia 10 (4), 39–72.

Alsop, G.I., Weinberger, R., Levi, T., Marco, S., 2016. Cycles of passive versus active diapirism recorded along an exposed salt wall. J. Struct. Geol. 84, 47–67. https://doi.org/10.1016/j.jsg.2016.01.008.

Ayala, C., Rey-Moral, C., Rubio, F., Soto, R., Clariana, P., Martín-León, J., Bellmunt, F., Gabàs, A., Macau, A., Casas, A.M., Martí, J., Pueyo, E.L., Benjumea, B., 2021. Gravity data on the Central Pyrenees: a step forward to help a better understanding of the Pyrenean structures. J. Maps 17 (2), 750–759. https://doi.org/10.1080/17445647.2021.2001386.

Bahroudi, A., Koyi, H., 2003. Effect of spatial distribution of Hormuz salt on deformation style in the Zagros fold and thrust belt: an analogue modelling approach. J. Geol. Soc. 160 (5), 719–733.

Beaumont, C., Muñoz, J.A., Hamilton, J., Fullsack, P., 2000. Factors controlling the alpine evolution of the central pyrenees inferred from a comparison of observations and geodynamical models. J. Geophys. Res. Solid Earth 105 (B4), 8121–8145. https://doi.org/10.1029/1999jb900390.

Buisson, C., Merle, O., 2002. Experiments on internal strain in lava dome cross sections. Bull. Volcanol. 64 (6), 363–371. https://doi.org/10.1007/s00445-002-0213-6.

Buisson, Cécile, Merle, O., 2004. Numerical simulation of strain within lava domes. J. Struct. Geol. 26 (5), 847–853. https://doi.org/10.1016/j.jsg.2003.11.017.

Burliga, S., 1996. Kinematics within the Kłodawa salt diapir, central Poland. Geol. Soc., London, Special Publ. 100 (1), 11–21. https://doi.org/10.1144/gsl.sp.1996.100.01.02.

Burliga, S., Janiów, S., Sadowski, A., 2005. Mining perspectives in the Klodawa salt mine considering modern knowledge on tectonics of the Klodawa salt structure. Technika Poszukiwan Geol. Geosynoptyka i Geotermia 4, 17–25.

Burrel, L., Teixell, A., 2021. Contractional salt tectonics and role of pre-existing diapiric structures in the southern pyrenean foreland fold–thrust belt (MONTSEC and serres marginals). J. Geol. Soc. 178 (4) https://doi.org/10.1144/jgs2020-085.

Calvet, F., Anglada, E., Salvany, J.M., 2004. El Triásico de los Pirineos. In: Vera, J.A. (Ed.), Geología de España, 272–274. Sociedad Geológica de España and Instituto Geológico y Minero de España.

Camara, P., Flinch, J., 2017. The Southern Pyrenees: a salt-based fold and thrust belt. Tectonics and Hydrocarbon Potential. In: Soto, J.I., Flinch, J.F., Tari, G. (Eds.), Permo-Triassic Salt Provinces of Europe, North Africa and the Atlantic Margins. Elsevier, pp. 395–415. https://doi.org/10.1016/B978-0-12-809417-4.00019-7.

Cartwright, J., Jackson, M., Dooley, T., Higgins, S., 2012. Strain partitioning in gravity-driven shortening of a thick, multilayered evaporite sequence. Geol. Soc., London, Special Publ. 363 (1), 449–470. https://doi.org/10.1144/sp363.21.

Casini, G., Vergés, J., Drzewiecki, P., Ford, M., Cruset, D., Wright, W., Hunt, D., 2023. Reconstructing the iberian salt-bearing rifted margin of the southern pyrenees: insights from the Organyà basin. Tectonics 42 (7). https://doi.org/10.1029/2022tc007715.

Chemia, Z., Koyi, H., 2008. The control of salt supply on entrainment of an anhydrite layer within a Salt Diapir. J. Struct. Geol. 30 (9), 1192–1200. https://doi.org/10.1016/j.jsg.2008.06.004.

Chemia, Z., Koyi, H., Schmeling, H., 2008. Numerical modelling of rise and fall of a dense layer in salt diapirs. Geophys. J. Int. 172, 798–816. https://doi.org/10.1111/j.1365-246X.2007.03661.x.

Chevrot, S., Sylvander, M., Diaz, J., Ruiz, M., Paul, A., 2015. The pyrenean architecture as revealed by Teleseismic P-to-s converted waves recorded along two dense transects. Geophys. J. Int. 200 (2), 1094–1105. https://doi.org/10.1093/gji/ggu400.

Cofrade, G., Cantarero, I., Gratacós, Ò., Ferrer, O., Ramirez-Perez, P., Travé, A., Roca, E., 2023a. Allochthonous salt advance recorded by the adjacent syn-kinematic sedimentation: example from the Les Avellanes Diapir (south central pyrenees). Global Planet. Change 220, 104020. https://doi.org/10.1016/j.gloplacha.2022.104020.

Cofrade, G., Gratacós, Ò., Cantarero, I., Ferrer, O., Ramirez-Perez, P., Roca, E., Travé, A., 2022. Les Avellanes Diapir, South-Central Pyrenees: reconstructing the kinematics of a salt diapir inside a fold-and-thrust belt. Preliminary results. 2nd Mediterranean Geosciences Union Annual Meeting (MedGu 2022) Abstract Book, pp. 430–431.

Cofrade, G., Gratacós, Ò., Cantarero, I., Ramirez-Perez, P., Ferrer, O., Roca, E., Travé, A., 2023b. Salt sheet extrusion and emplacement within the South-Central Pyrenean fold-and-thrust belt: the Les Avellanes Diapir case study. J. Maps (in press).

Cosgrove, J.W., Talbot, C.J., Aftabi, P., 2009. A train of kink folds in the surficial salt of Qom Kuh, Central Iran. J. Struct. Geol. 31 (10), 1212–1222. https://doi.org/10.1016/j.jsg.2009.06.014.

Cruset, D., Vergés, J., Albert, R., Gerdes, A., Benedicto, A., Cantarero, I., Travé, A., 2020. Quantifying deformation processes in the SE Pyrenees using U–Pb dating of fracture-filling calcites. J. Geol. Soc. 177 (6), 1186–1196. https://doi.org/10.1144/jgs2020-014.

de Oliveira Santos, C.H., Pichel, L.M., Alves Da Silva, F.C., 2023. The effects of subsalt relief on gravity-driven salt tectonics: results from analogue modelling. J. Struct. Geol. 174, 104919 https://doi.org/10.1016/j.jsg.2023.104919.

Dooley, T.P., Hudec, M.R., Carruthers, D., Jackson, M.P., Luo, G., 2017. The effects of base-salt relief on salt flow and suprasalt deformation patterns—Part 1: flow across simple steps in the base of salt. Interpretation 5 (1). https://doi.org/10.1190/INT-2016-0087.1. SD1–SD23.

Dooley, T.P., Jackson, M.P., Hudec, M.R., 2015. Breakout of squeezed stocks: dispersal of roof fragments, source of extrusive salt and interaction with regional thrust faults. Basin Res. 27 (1), 3–25. https://doi.org/10.1111/bre.12056.

Dooley, T., McClay, K.R., Hempton, M., Smit, D., 2005. Salt tectonics above complex basement extensional fault systems: results from analogue modelling. Petrol. Geol. Conf. Ser. 6 (1), 1631–1648. https://doi.org/10.1144/0061631.

Duffy, O.B., Dooley, T.P., Hudec, M.R., Jackson, M.P.A., Fernandez, N., Jackson, C.A.-L., Soto, J.I., 2018. Structural evolution of salt-influenced fold-and-thrust belts: a synthesis and new insights from basins containing isolated salt diapirs. J. Struct. Geol. 114, 206–221. https://doi.org/10.1016/j.jsg.2018.06.024.

Escher, B.G., Kuenen, Ph H., 1929. Experiments in connection with salt domes. Leidse Geol. Meded. 3 (1), 151–182.

Evans, S.L., Jackson, C.A.-L., 2021. Intra-salt structure and strain partitioning in layered evaporites: implications for drilling through Messinian Salt in the Eastern Mediterranean. Petrol. Geosci. 27 (4) https://doi.org/10.1144/petgeo2020-072.

Faramarzi, N.S., Amini, S., Schmitt, A.K., Hassanzadeh, J., Borg, G., McKeegan, K., Razavi, S.M., Mortazavi, S.M., 2015. Geochronology and geochemistry of rhyolites from hormuz island, southern Iran: a new record of cadomian arc magmatism in the hormuz formation. Lithos 236–237, 203–211. https://doi.org/10.1016/j.lithos.2015.08.017.

Fiduk, J.C., Rowan, M.G., 2012. Analysis of folding and deformation within layered evaporites in Blocks BM-S-8 & -9, Santos Basin, Brazil. In: Alsop, G.I., Archer, S.G., Hartley, A.J., Grant, N.T., Hodgkinson, R. (Eds.), Salt Tectonics, Sediments and Prospectivity, vol. 363. Geol. Soc. London Spec. Publ., pp. 471–487. https://doi.org/10.1144/SP363.22

Fillon, C., Gautheron, C., Van der Beek, P., 2013. Oligocene–Miocene burial and exhumation of the Southern Pyrenean foreland quantified by low-temperature thermochronology. J. Geol. Soc. 170 (1), 67–77. https://doi.org/10.6084/m9.figshare.3453161.v1.

Frumkin, A., Pe'eri, S., Zak, I., 2021. Development of banded terrain in an active salt diapir: potential analog to Mars. Geomorphology 389, 107824. https://doi.org/10.1016/j.geomorph.2021.107824.

Fuchs, L., Koyi, H., Schmeling, H., 2015. Numerical modeling of the effect of composite rheology on internal deformation in down-built diapirs. Tectonophysics 646, 79–95. https://doi.org/10.1016/j.tecto.2015.01.014.

Garcés, M., López-Blanco, M., Valero, L., Beamud, E., Muñoz, J.A., Oliva-Urcia, B., Vinyoles, A., Arbués, P., Cabello, P., Cabrera, L., 2020. Paleogeographic and sedimentary evolution of the south Pyrenean foreland basin. Mar. Petrol. Geol. 113, 104105 https://doi.org/10.1016/j.marpetgeo.2019.104105.

García-Senz, J., 2002. Cuencas extensivas del Cretácico Inferior en los Pirineos centrales. Formación y subsecuente inversión. Tesis Doctoral. Universitat de Barcelona. http://hdl.handle.net/10803/1913.

González-Esvertit, E., Alcalde, J., Gomez-Rivas, E., 2023. IESDB – the Iberian Evaporite Structure Database. https://doi.org/10.5194/essd-2022-340.

González-Esvertit, E., Canals, À., Bons, P.D., Murta, H., Casas, J.M., Gomez-Rivas, E., 2022. Geology of giant quartz veins and their host rocks from the Eastern Pyrenees (Southwest Europe). J. Maps 1–13. https://doi.org/10.1080/17445647.2022.2133642.

Hudec, M.R., Dooley, T.P., Burrel, L., Teixell, A., Fernandez, N., 2021. An alternative model for the role of salt depositional configuration and preexisting salt structures in the evolution of the Southern Pyrenees, Spain. J. Struct. Geol. 146, 104325 https://doi.org/10.1016/j.jsg.2021.104325.

Hudec, M.R., Jackson, M.P.A., 2006. Advance of allochthonous salt sheets in passive margins and orogens. AAPG Bull. 90 (10), 1535–1564. https://doi.org/10.1306/05080605143.

Hudec, M.R., Jackson, M.P.A., 2007. Terra infirma: understanding salt tectonics. Earth Sci. Rev. 82 (1–2), 1–28. https://doi.org/10.1016/j.earscirev.2007.01.001.

Hudson, S., Tuttle, T., Wood, M., 2017. Source within the seal—distribution and implications of organic shale-bearing stringers within the onion Creek diapir, northern paradox basin, Utah. Geol. Intermountain West 4, 215–229. https://doi.org/10.31711/giw.v4.pp215-229.

Jackson, C.A.-L., Jackson, M.P.A., Hudec, M.R., Rodriguez, C., 2014. Internal structure, Kinematics, and growth of a salt wall: insights from 3-D seismic data. Geology 42 (4), 307–310. https://doi.org/10.1130/g34865.1.

Jackson, C.A.-L., Lewis, M.M., 2012. Origin of an anhydrite sheath encircling a salt diapir and implications for the seismic imaging of steep-sided salt structures, Egersund Basin, northern North Sea. J. Geol. Soc. 169 (5), 593–599. https://doi.org/10.1144/0016-76492011-126.

Jackson, C.A.-L., Stewart, S.A., 2017. Composition, tectonics, and hydrocarbon significance of Zechstein supergroup salt on the United Kingdom and Norwegian Continental shelves. In: Permo-Triassic Salt Provinces of Europe, North Africa and the Atlantic Margins, pp. 175–201. https://doi.org/10.1016/b978-0-12-809417-4.00009-4.

Jackson, C., Jackson, M., Hudec, M., Rodriguez, C., 2015. Enigmatic structures within salt walls of the Santos Basin—part 1: geometry and kinematics from 3D seismic reflection and well data. J. Struct. Geol. 75, 135–162. https://doi.org/10.1016/j.jsg.2015.01.010.

Jackson, M., Hudec, M., 2017a. Salt structures. In: Salt Tectonics: Principles and Practice. Cambridge University Press, Cambridge, pp. 61–254. https://doi.org/10.1017/9781139003988.006.

Jackson, M., Hudec, M., 2017b. Internal deformation in salt bodies. In: Salt Tectonics: Principles and Practice. Cambridge University Press, Cambridge, pp. 181–228. https://doi.org/10.1017/9781139003988.011.

Jurado, M.J., 1990. El triásico y el liásico basal evaporíticos del subsuelo de la cuenca del Ebro. In: Ortí, F., Salvany, J.M. (Eds.), Formaciones evaporíticas de la Cuenca del Ebro y cadenas periféricas, y de la zona de Levante. Nuevas aportaciones y guía de superficie.

Kernen, R.A., Giles, K.A., Poe, P.L., Gannaway Dalton, C.E., Rowan, M.G., Fiduk, J.C., Hearon, T.E., 2019. Origin of the neoproterozoic rim dolomite as lateral carbonate caprock, Patawarta salt sheet, Flinders Ranges, South Australia. Aust. J. Earth Sci. 67 (6), 815–832. https://doi.org/10.1080/08120099.2019.1588695.

Klimowitz, J., Torrescusa, S., 1990. Notas sobre la estratigrafía y facies de la serie triásica en et Alóctono Surpirenico. In: ORTI, F., SALVANY, J.M. (Eds.), Formaciones evaporíticas de la Cuenca del Ebro y cadenas periféricas, y de la zona de Levante. Nuevas aportaciones y guía de superficie. ENRESA and GPPG, Barcelona, pp. 29–33.

Koyi, H., 1998. The shaping of salt diapirs. J. Struct. Geol. 20 (4), 321–338. https://doi.org/10.1016/s0191-8141(97)00092-8.

Koyi, H.A., 2001. Modeling the influence of sinking anhydrite blocks on salt diapirs targeted for hazardous waste disposal. Geology 29 (5), 387. https://doi.org/10.1130/0091-7613(2001)029<0387:mtiosa>2.0.co, 2.

Krýza, O., Lexa, O., Schulmann, K., Guy, A., Gapais, D., Cosgrove, J., Xiao, W., 2021. Oroclinal buckling and associated lithospheric-scale material flow–insights from physical modelling: implication for the Mongol-Hingan orocline. Tectonophysics 800, 228712.

Krýza, O., Závada, P., Lexa, O., 2019. Advanced strain and mass transfer analysis in crustal-scale oroclinal buckling and detachment folding analogue models. Tectonophysics 764, 88–109.

Krýza, O., Závada, P., Shu, T., Semerád, J., 2022. Modes and geometry of crustal-scale detachment folding in hot orogens—insights from physical modeling. Front. Earth Sci. 10, 965497.

Lago-San José, M., Arranz-Yagüe, E., Bastida-Cuairan, J., Galé-Bornao, C., 1999. Las doleritas toleíticas triásicas del sector SE de la Cordillera Ibérica: petrología y geoquímica. ISSN 0367-0449, (55)5-6 Estudios geológicos 223–236.

Lanaja, J.M., 1987. Contribución de la exploración petrolífera al conocimiento de la geología de España. In: Edt. IGME and Universidad Politécnica de, Madrid. ISBN 8474743982.

Leach, D.L., Song, Y.-C., Hou, Z.-Q., 2016. The world-class jinding Zn–PB deposit: ore formation in an evaporite dome, Lanping basin, Yunnan, China. Miner. Deposita 52 (3), 281–296. https://doi.org/10.1007/s00126-016-0668-6.

Li, S., 2012. Numerical studies of the deformation of salt bodies with embedded carbonate stringers. Doctoral Thesis. In: Faculty of Georesources and Materials Engineering of the RWTH Aachen University.

Li, S., Abe, S., Reuning, L., Becker, S., Urai, J.L., Kukla, P.A., 2012. Numerical modeling of the displacement and deformation of embedded rock bodies during salt tectonics - a case study from the South Oman Salt Basin. In: Alsop, I. (Ed.), Salt Tectonics, Sediments and Prospectivity, vol. 363. Geological Society Special Publication, pp. 503–520.

López-Gómez, J., et al., 2019. Permian-triassic rifting stage. In: Quesada, C., Oliveira, J. (Eds.), The Geology of Iberia: A Geodynamic Approach. Regional Geology Reviews. Springer, Cham. https://doi.org/10.1007/978-3-030-11295-0_3.

Lopez-Mir, B., Muñoz, J.A., García-Senz, J., 2015. Extensional salt tectonics in the partially inverted Cotiella post-rift basin (south-central Pyrenees): structure and evolution. Int. J. Earth Sci. 104 (2), 419–434. https://doi.org/10.1007/s00531-014-1091-9.

Lopez-Mir, B., Muñoz, J.A., García-Senz, J., 2016. Geology of the cotiella thrust sheet, southern pyrenees (Spain). J. Maps 12 (Suppl. 1), 323–327. https://doi.org/10.1080/17445647.2016.1211895.

Martín-Martín, J.D., Vergés, J., Saura, E., Moragas, M., Messager, G., Baqués, V., Razin, P., Grélaud, C., Malaval, M., Joussiaume, R., Casciello, E., Cruz-Orosa, I., Hunt, D.W., 2017. Diapiric growth within an early jurassic rift basin: the Tazoult Salt Wall (central high atlas, Morocco). Tectonics 36 (1), 2–32. https://doi.org/10.1002/2016tc004300.

McGuiness, D.B., Hossack, J.R., Zellers, S., Silva, H.T.D., 1993. The development of allochthonous salt sheets as controlled by the rates of extension, sedimentation, and salt supply, 127–139. In: Rates of Geologic Processes, Tectonics, Sedimentation, Eustasy and Climate - Implications for Hydrocarbon Exploration: 14th Annual. https://doi.org/10.5724/gcs.93.14.0127.

Muñoz, J.A., 1992. Evolution of a continental collision belt: ECORS-pyrenees crustal balanced cross-section. Thrust Tectonics 235–246. https://doi.org/10.1007/978-94-011-3066-0_21.

Muñoz, J.A., 2002. The pyrenees. In: Gibbons, W., Moreno, T. (Eds.), The Geology of Spain. Geological Society, London, pp. 370–385, 2002.

Muñoz, J.A., 2017. Fault-Related folds in the southern pyrenees. AAPG Bull. 101, 579–587. https://doi.org/10.1306/011817dig17037, 04.

Muñoz, J.A., Beamud, E., Fernández, O., Arbués, P., Dinarès-Turell, J., Poblet, J., 2013. The ainsa fold and thrust oblique zone of the central pyrenees: kinematics of a curved contractional system from paleomagnetic and Structural Data. Tectonics 32 (5), 1142–1175. https://doi.org/10.1002/tect.20070.

Muñoz, J.A., Mencos, J., Roca, E., Carrera, N., Gratacós, O., Ferrer, O., Fernández, O., 2018. The Structure of the South-Central-Pyrenean fold and thrust belt as

constrained by subsurface data. Geol. Acta 16 (4), 439–460. https://doi.org/10.1344/GeologicaActa2018.16.4.7.
Muñoz-López, D., Cruset, D., Vergés, J., Cantarero, I., Benedicto, A., Mangenot, X., Albert, R., Gerdes, A., Beranoaguirre, A., Travé, A., 2022. Spatio-temporal variation of fluid flow behavior along a fold: the bóixols-sant corneli anticline (southern Pyrenees) from U–pb dating and structural, petrographic and geochemical constraints. Mar. Petrol. Geol. 143, 105788 https://doi.org/10.1016/j.marpetgeo.2022.105788.
Ortí, F., García-Veigas, J., Rosell, L., Jurado, M.J., Utrilla, R., 1996. Formaciones salinas de las cuencas triásicas en la Península Ibérica: caracterización petrológica y geoquímica. Cuad. Geol. Iber. 20, 13–35.
Pedreira, D., Pulgar, J.A., Gallart, J., Díaz, J., 2003. Seismic evidence of Alpine crustal thickening and wedging from the western Pyrenees to the Cantabrian Mountains (north Iberia). J. Geophys. Res. 108 (B4), 2204. https://doi.org/10.1029/2001JB001667.
Peel, F.J., Hudec, M.R., Weijermars, R., 2020. Salt Diapir downbuilding: fast analytical models based on rates of salt supply and sedimentation. J. Struct. Geol. 141, 104202 https://doi.org/10.1016/j.jsg.2020.104202.
Pichel, M., Finch, L., Gawthorpe, R.L., 2019. The impact of Pre-Salt Rift Topography on salt tectonics: a discrete-element modeling approach. Tectonics 38 (4), 1466–1488. https://doi.org/10.1029/2018tc005174.
Pla, O., Roca, E., Xie, H., Izquierdo-Llavall, E., Muñoz, J.A., Rowan, M.G., Ferrer, O., Gratacós, O., Yuan, N., Huang, S., 2019. Influence of syntectonic sedimentation and décollement rheology on the geometry and evolution of orogenic wedges: analog modeling of the Kuqa fold-and-thrust belt (NW China). Tectonics 38 (8), 2727–2755. https://doi.org/10.1029/2018TC005386.
Pocoví, A., 1978. Estudio geológico de las Sierras Marginales Catalanas (Prepirineo de Lérida) Tesis Doctoral (1978). Universitat de Barcelona.
Posey, H.H., Kyle, J.R., 1988. Fluid-rock interactions in the salt dome environment: an introduction and review. Chem. Geol. 74 (1–2), 1–24. https://doi.org/10.1016/0009-2541(88)90143-x.
Reuning, L., Johannes, S., Ansgar, H., Urai, J.L., Littke, R., Kukla, P.A., Rawahi, Z., 2009. Constraints on the diagenesis, stratigraphy and internal dynamics of the surface-piercing salt domes in the Ghaba Salt Basin (Oman): a comparison to the ARA Group in the South Oman Salt Basin. GeoArabia 14 (3), 83–120. https://doi.org/10.2113/geoarabia140383.
Roca, E., Ferrer, O., Rowan, M.G., Muñoz, J.A., Butillé, M., Giles, K.A., Arbués, P., de Matteis, M., 2021. Salt tectonics and controls on halokinetic-sequence development of an exposed deepwater diapir: the Bakio Diapir, Basque-cantabrian basin, Pyrenees. Mar. Petrol. Geol. 123, 104770 https://doi.org/10.1016/j.marpetgeo.2020.104770.
Rosenau, M., Warsitzka, M., Zavada, P., 2022. Ring-shear Test Data of Glass Beads 100-200 Mm Used for Analogue Experiments in the Tectonic Modelling Labs at GFZ Potsdam and the. Institute of Geophysics of the Czech Academy of Sciences, Prague.
Rowan, M.G., Urai, J.L., Fiduk, J.C., Kukla, P.A., 2019. Deformation of intrasalt competent layers in different modes of salt tectonics. Solid Earth 10 (3), 987–1013. https://doi.org/10.5194/se-10-987-2019.
Rowan, M., Fiduk, J., 2015. Internal Deformation in Layered Evaporite Sequences: Evacuation and Diapirism versus Contraction and Inflation. AAPG Annual Convention and Exhibition.
Rowan, M., Krzywiec, P., Bukowski, K., Przybylop, J., 2020. Nature and origin of large-scale and intrasalt deformation within the Wieliczka salt mine Poland. Geol. Q. 64 (4) https://doi.org/10.7306/gq.1557.
Salvany, J.M., Bastida, J.C., 2004. Análisis litoestratigráfico del Keuper Surpirenaico Central. Rev. Soc. Geol. Espana 17 (1–2), 3–26.
Santolaria, P., Casas-Sainz, A.M., Soto, R., Pinto, V., Casas, A., 2014. The Naval diapir (southern Pyrenees): geometry of a salt wall associated with thrusting at an oblique ramp. Tectonophysics 637, 30–44. https://doi.org/10.1016/j.tecto.2014.09.008.
Santolaria, P., Ferrer, O., Rowan, M.G., Snidero, M., Carrera, N., Granado, P., Muñoz, J. A., Roca, E., Schneider, C.L., Piña, A., Zamora, G., 2021. Influence of preexisting salt diapirs during thrust wedge evolution and secondary welding: insights from Analog Modeling. J. Struct. Geol. 149, 104374 https://doi.org/10.1016/j.jsg.2021.104374.
Santolaria, P., Rubio, F.M., Ayala, C., Pueyo, E.L., Rodríguez-Pintó, A., Soto, R., Casas, A. M., 2016. Gravimetría preliminar del antepaís Pirenaico central; distribución de las evaporitas y geometría de zócalo. Preliminary gravimetry in the central Pyrenean foreland; evaporite distribution and basement geometry. IX Congreso Geológico de España. ISSN 1576-5172 Geotemas 16 (2).
Sarkarinejad, K., Sarshar, M.A., Adineh, S., 2018. Structural, micro-structural and kinematic analyses of channel flow in the Karmostaj salt diapir in the Zagros foreland folded belt, fars Province, Iran. J. Struct. Geol. 107, 109–131. https://doi.org/10.1016/j.jsg.2017.12.005.
Saura, E., Ardèvol i Oró, L., Teixell, A., Vergés, J., 2016. Rising and falling diapirs, shifting depocenters, and flap overturning in the cretaceous Sopeira and sant Gervàs subbasins (ribagorça basin, southern pyrenees). Tectonics 35 (3), 638–662. https://doi.org/10.1002/2015tc004001.
Schléder, Z., Urai, J.L., Nollet, S., Hilgers, C., 2008. Solution-precipitation creep and fluid flow in halite: a case study of Zechstein (z1) rocksalt from Neuhof salt mine (Germany). Int. J. Earth Sci. 97 (5), 1045e1056.
Schoenherr, J., Schléderr, Z., Urai, J.L., Littke, R., Kukla, P.A., 2010. Deformation mechanisms of deeply buried and surface-piercing late pre-cambrian to early cambrian Ara salt from interior Oman. Int. J. Earth Sci. 99 (5), 1007e1025.
Séguret, M., 1972. Étude tectonique des nappes et séries décollées de la partie centrale du versant sud des Pyrénées – caractère synsédimentaire, rôle de la compression et de la gravité. Publications de l'Universite des Sciences et Techniques du Languedoc (USTELA), Montpellier, France (1972). Série Géol. Struct. 2, 155.
Strozyk, F., 2017. The internal structure of the zechstein salt and related drilling risks in the Northern Netherlands. Permo-Triassic Salt Provinces of Europe, 115–128. In: North Africa and the Atlantic Margins. https://doi.org/10.1016/b978-0-12-809417-4.00006-9.
Strozyk, F., van Gent, H., Urai, J.L., Kukla, P.A., 2012. 3D seismic study of complex intra-salt deformation: an example from the Zechstein 3 stringer in the western Dutch offshore. In: Alsop, I. (Ed.), Salt Tectonics, Sediments and Prospectivity, vol. 363. Geological Society Special Publication, pp. 489–502.
Talbot, C., 1979. Fold trains in a glacier of salt in southern Iran. J. Struct. Geol. 1 (1), 5–18. https://doi.org/10.1016/0191-8141(79)90017-8.
Talbot, C.J., Pohjola, V., 2009. Subaerial salt extrusions in Iran as analogues of ice sheets, streams and glaciers. Earth Sci. Rev. 97 (1–4), 155–183. https://doi.org/10.1016/j.earscirev.2009.09.004.
Talbot, C., Jackson, M., 1987. Internal kinematics of salt diapirs. AAPG Bull. 71 (9), 1068–1093.
Talbot, C., Aftabi, P., 2004. Geology and models of salt extrusion at Qum Kuh, central Iran. J. Geol. Soc. 161 (2), 321–334. https://doi.org/10.1144/0016-764903-102.
Talbot, C.J., Medvedev, S., Alavi, M., Shahrivar, H., Heidari, E., 1999. Salt extrusion at Kuh-e-Jahani, Iran, from June 1994 to November 1997. Geol. Soc. Lond., Spec. Publ. 174 (1), 93–110. https://doi.org/10.1144/GSL.SP.1999.174.01.06.
Teixell, A., Muñoz, J.A., 2000. Evolución tectono-sedimentaria del Pirineo meridional durante el Terciario: una síntesis basada en la transversal del río Noguera Ribagorçana. Rev. Soc. Geol. Espana 13 (2), 251–264.
Teixell, A., Barnolas, A., 1995. Significado de la discordancia de Mediano en relación con las estructuras adyacentes (Pirineo central). Geogaceta 17, 186–189.
Ullastre, J., Masriera, A., 2004. Sobre la edad de los conglomerados basales de la transgresión del Senoniense en la parte más interna de la cuenca sudpirenaica catalana (NE de España). Treballs Museu Geol. Barcelona 2004 (12), 175–185. https://raco.cat/index.php/TreballsMGB/article/view/72455.
Van Gent, H., Urai, J.L., De Keijzer, M., 2011. The internal geometry of salt structures - a first look using 3D seismic data from the Zechstein of The Netherlands. J. Struct. Geol. 33, 292–311.
Vergés, J., Fernàndez, M., Martìnez, A., 2002. The pyrenean orogen: pre-, syn-, and post-collisional evolution, 08 J. Virtual Explor.. https://doi.org/10.3809/jvirtex.2002.00058.
Vergés, J., Muñoz, J.A., 1990. Thrust sequence in the southern central pyrenees. Bull. Soc. Geol. Fr. VI (2), 265–271. https://doi.org/10.2113/gssgfbull.vi.2.265.
Warren, J.K., 2010. Evaporites through time: tectonic, climatic and eustatic controls in marine and nonmarine deposits. Earth Sci. Rev. 98 (3–4), 217–268. https://doi.org/10.1016/j.earscirev.2009.11.004.
Warren, J.K., 2016. Evaporites a Geological Compendium. Springer International Publishing.
Warsitzka, M., Kley, J., Kukowski, N., 2013. Salt diapirism driven by differential loading—some insights from analogue modelling. Tectonophysics 591, 83–97.
Warsitzka, M., Kley, J., Kukowski, N., 2015. Analogue experiments of salt flow and pillow growth due to basement faulting and differential loading. Solid Earth 6 (1), 9–31. https://doi.org/10.5194/se-6-9-2015.
Warsitzka, M., Závada, P., Jähne-Klingberg, F., Krzywiec, P., 2021a. Contribution of gravity gliding in salt-bearing rift basins – a new experimental setup for simulating salt tectonics under the influence of sub-salt extension and tilting. Solid Earth 12 (8), 1987–2020. https://doi.org/10.5194/se-12-1987-2021.
Warsitzka, M., Závada, P., Krýza, O., Pohlenz, A., Rosenau, M., 2021b. Ring-shear Test Data of Quartz Sand–Silicate Cenospheres Mixtures Used for Analogue Experiments at the Institute of Geophysics of the Czech Academy of Science, Prague.
Weijermars, R., Schmeling, H., 1986. Scaling of Newtonian and non-Newtonian fluid dynamics without inertia for quantitative modelling of rock flow due to gravity (including the concept of rheological similarity). Phys. Earth Planet. In. 43 (4), 316–330.
Yin, H., Groshong, R.H., 2007. A three-dimensional kinematic model for the deformation above an active diapir. AAPG Bull. 91 (3), 343–363. https://doi.org/10.1306/10240606034.
Závada, P., Bruthans, J., Adineh, S., Warsitzka, M., Zare, M., 2021. Composition and deformation patterns of the caprock on salt extrusions in southern Iran – field study on the Karmostaj and Siah Taq diapirs. J. Struct. Geol. 151, 104422 https://doi.org/10.1016/j.jsg.2021.104422.
Závada, P., Stanĕk, M., Machek, M., Géraud, Y., Bruthans, J., Soraya, A., 2023. Microporosity Evolution of Naturally Deformed Caprock on Salt Diapirs in Southern Iran. https://doi.org/10.5194/egusphere-egu23-11382.